

FACULTY
OF MATHEMATICS
AND PHYSICS
Charles University

1

BACHELOR THESIS

2

Martin Vavřík

3

**Simulation and Reconstruction
of Charged Particle Trajectories
in an Atypic Time Projection Chamber**

4

5

Institute of Particle and Nuclear Physics

6

Supervisor of the bachelor thesis: Mgr. Tomáš Sýkora, Ph.D.

7

Study programme: Physics

8

Prague 2025

- ⁹ I declare that I carried out this bachelor thesis independently, and only with the
¹⁰ cited sources, literature and other professional sources. It has not been used to
¹¹ obtain another or the same degree.
- ¹² I understand that my work relates to the rights and obligations under the Act
¹³ No. 121/2000 Sb., the Copyright Act, as amended, in particular the fact that the
¹⁴ Charles University has the right to conclude a license agreement on the use of this
¹⁵ work as a school work pursuant to Section 60 subsection 1 of the Copyright Act.

In date
Author's signature

Title: Simulation and Reconstruction of Charged Particle Trajectories in an Atypical Time Projection Chamber **Added hyphen to avoid overfull hbox**

Author: Martin Vavřík

Institute: Institute of Particle and Nuclear Physics

Supervisor: Mgr. Tomáš Sýkora, Ph.D., Institute of Particle and Nuclear Physics

Abstract: Abstract.

Keywords: key words

¹⁷ Contents

¹⁸	Motivation	³
¹⁹	0.1 ATOMKI Anomaly	³
²⁰	0.1.1 ATOMKI Measurements	³
²¹	0.1.2 Other Experiments	⁴
²²	0.2 X17 Project at IEAP CTU	⁷
²³	1 Time Projection Chamber	⁹
²⁴	1.1 Charge transport in gases	⁹
²⁵	1.1.1 Drift	¹⁰
²⁶	1.1.2 Diffusion	¹¹
²⁷	1.2 Examples of Time Projection Chambers (TPCs)	¹²
²⁸	1.2.1 The original TPC at PEP-4 at SLAC	¹²
²⁹	1.2.2 The ALICE TPC	¹²
³⁰	1.2.3 The CERES/NA45 radial drift TPC	¹²
³¹	1.3 Readout	¹³
³²	1.3.1 Multi-Wire Proportional Chamber	¹³
³³	1.3.2 Micro-Pattern Gaseous Detectors	¹³
³⁴	1.4 Orthogonal Fields TPC at IEAP CTU	¹⁵
³⁵	1.4.1 Motivation and Associated Challenges	¹⁶
³⁶	1.4.2 Coordinate Systems and Dimensions	¹⁶
³⁷	1.4.3 Magnetic Field Simulation	¹⁸
³⁸	2 Track Simulation	²²
³⁹	2.1 Microscopic Simulation	²²
⁴⁰	2.1.1 First testing track	²³
⁴¹	2.1.2 Grid-like testing sample	²³
⁴²	2.2 Runge-Kutta Simulation	²³
⁴³	2.2.1 Testing sample	²⁶
⁴⁴	3 Track Reconstruction	²⁸
⁴⁵	3.1 Reconstruction Assuming Steady Drift	²⁸
⁴⁶	3.2 Ionization Electron Map	²⁹
⁴⁷	3.2.1 Gradient Descent Algorithm	³⁶
⁴⁸	3.2.2 Interpolation on the Inverse Grid	³⁷
⁴⁹	3.3 Discrete Reconstruction	³⁹
⁵⁰	4 Energy Reconstruction	⁴¹
⁵¹	4.1 Cubic Spline Fit	⁴¹
⁵²	4.2 Circle and Lines Fit	⁴³
⁵³	4.2.1 Two-dimensional fit	⁴⁴
⁵⁴	4.2.2 Three-dimensional fit	⁴⁵
⁵⁵	4.2.3 Testing on a Runge-Kutta sample	⁴⁷
⁵⁶	4.3 Runge-Kutta Fit	⁴⁸
⁵⁷	4.3.1 Testing on a microscopic sample	⁵⁰
⁵⁸	Conclusion	⁵²

59	Bibliography	56
60	List of Abbreviations	63

61 Motivation

62 Or chapter 1? MFF UK thesis template uses Introduction as an unnumbered
63 chapter, but it's not clear how they handle numbering inside the chapter. A TPC [refs]
64 is a gaseous detector that reconstructs charged particle trajectories by measuring
65 the positions and drift times of ionization electrons (and sometimes also ions) cre-
66 ated in the gas. The energies of these particles can be inferred from the curvatures
67 of their trajectories in a magnetic field.

68 The goal of this thesis is to develop an algorithm for the reconstruction of
69 charged particle trajectories and energy in an *atypic* TPC with orthogonal elec-
70 tric and magnetic fields, hereafter referred to as the Orthogonal Fields TPC
71 (OFTPC), used in the X17 project at the Institute of Experimental and Ap-
72 plied Physics, Czech Technical University in Prague (IEAP CTU). Furthermore,
73 we present the results of testing of several (gradually improving) developed algo-
74 rithms with different samples of simulated data. Put this somewhere, (maybe just
75 the abstract?). We use the Garfield++ toolkit [1] for simulations in combination
76 with the ROOT framework [2] for data analysis and visualization. Some of our
77 more demanding simulations are run on the MetaCentrum grid [3].

78 The X17 project in IEAP CTU aims to reproduce measurements of anomalous
79 behavior in the angular correlation distribution of pairs produced by the Internal
80 Pair Creation (IPC) mechanism [4] during the decay of certain excited nuclei
81 (^{8}Be , ^{12}C , and ^{4}He) observed by a team at ATOMKI in Hungary. I would leave
82 this here as a short summary before I explain it in more detail in the sections
83 below.

84 Add citations: X17 project, VdG. Maybe also TPC, etc.

85 0.1 ATOMKI Anomaly

86 Many different theories propose the existence of *new light boson(s)* that are weakly
87 coupled to ordinary matter [5]. These particles are potential dark matter candi-
88 dates and could contribute to a solution of other issues with the Standard Model,
89 such as the strong CP problem¹ and the anomalous muon magnetic moment. Mass
90 range of axions?

91 A possible way of detecting such bosons with a short lifetime is to observe
92 nuclear transitions of excited nuclei. If a boson was emitted during the transition
93 and subsequently decayed into an electron-positron pair, we could observe this as
94 a peak on top of the standard e^+e^- (both cursive and upright forms are used in
95 different articles) angular correlation from the Internal Pair Creation (IPC) and
96 the External Pair Creation (EPC).

97 0.1.1 ATOMKI Measurements

98 Historically, there were several measurements of the IPC in nuclear transitions
99 in ^{8}Be at Institute für Kernphysik (Frankfurt) [6, 7, 8] and at ATOMKI (Debre-
100 cen, Hungary) [9, 10] resulting in different anomalies with invariant mass in the

¹The CP symmetry could be violated in strong interactions according to the current formulation of quantum chromodynamics, but no such violation is observed.

range 5 – 15 MeV. This motivated the development of a better spectrometer at ATOMKI.

In 2015, a group at ATOMKI observed an anomalous IPC in ${}^8\text{Be}$ [11]. They used the ${}^7\text{Li}(p, \gamma){}^8\text{Be}$ reaction at the $E_p = 1030$ keV proton capture resonance to prepare the 18.15 MeV excited state ($J^\pi = 1^+, T = 0$). This state decays predominantly through M1 transitions to the ground state ($J^\pi = 0^+, T = 0$) and to the 3.03 MeV state ($J^\pi = 2^+, T = 0$) [12]. **Transition figure – all transitions of isotopes? IPC figure?**

The angular correlation of the e^+e^- pairs created internally in these transitions were measured and compared to the simulation; results from a narrow $E_{\text{sum}} = 18$ MeV region are shown in Fig. 0.1a. The simulation includes boson decay pairs for different boson masses. The disparity parameter y is used to describe the asymmetry of energy between the two particles. It is defined as

$$y = \frac{E_{e^-} - E_{e^+}}{E_{e^-} + E_{e^+}}, \quad (0.1)$$

where E_{e^-} and E_{e^+} are the kinetic energies of the electron and positron.

Their experimental setup was later upgraded (**details?**) and used for new measurements. In 2022 the ${}^8\text{Be}$ anomaly was also measured using the $E_p = 441$ keV resonance to produce the 17.64 MeV excited state ($J^\pi = 1^+, T = 1$) which again decays primarily to the ground state and the 3.03 MeV state [12]. The anomaly was also verified for $E_p = 650$ and 800 keV where E1 transitions from the direct proton capture dominate [13]. The results for e^+e^- with $E_{\text{sum}} \in [13.5, 20]$ MeV are shown in Fig. 0.1b.

The newer setup was also used in 2021 to study the ${}^3\text{H}(p, e^+e^-){}^4\text{He}$ reaction at $E_p = 510, 610$ and 900 keV [14], inducing direct and resonant capture populating the overlapping first 20.21 MeV ($J^\pi = 0^+$) and second 21.01 MeV ($J^\pi = 0^-$) excited states [15]. The comparison of simulated and measured e^+e^- pair angular correlations in the $E_{\text{sum}} \in [18, 22]$ MeV region is shown in Fig. 0.1c.

In 2022, another anomaly was measured in the ${}^{11}\text{B}(p, e^+e^-){}^{12}\text{C}$ process [16]. The $E_p = 1388$ keV resonance was used to populate the 17.23 MeV excited state ($J^\pi = 1^-, T = 1$) with a large width $\Gamma = 1.15$ MeV [17]. This state decays mainly through E1 transitions to the ground state $J^\pi = 0^+$ and to the 4.44 MeV state $J^\pi = 2^+$. To compensate for energy losses in the target, five energies in the range $E_p = 1.5\text{--}2.5$ MeV were used. The experimental angular correlation for the 17.23 MeV transition to the ground state is shown in Fig. 0.1d.

Possible explanations of the anomaly include experimental effects, higher order processes in the Standard Model [18, 19] or even a protophobic fifth force mediated by a new 17 MeV boson X17 [20]. **Not sure if the introduction should be referenced since even though it is related, it is an independent theory developed only (?) to explain these measurements. Zhang and Miller: <https://www.sciencedirect.com/science/article/pii/S0370269321000010>**

0.1.2 Other Experiments

Since the ATOMKI measurements, several experiments have been initiated to attempt to replicate the results and search for the hypothetical X17 particle. The following experiments have already produced results. **Could cite the ATOMKI review paper here.**

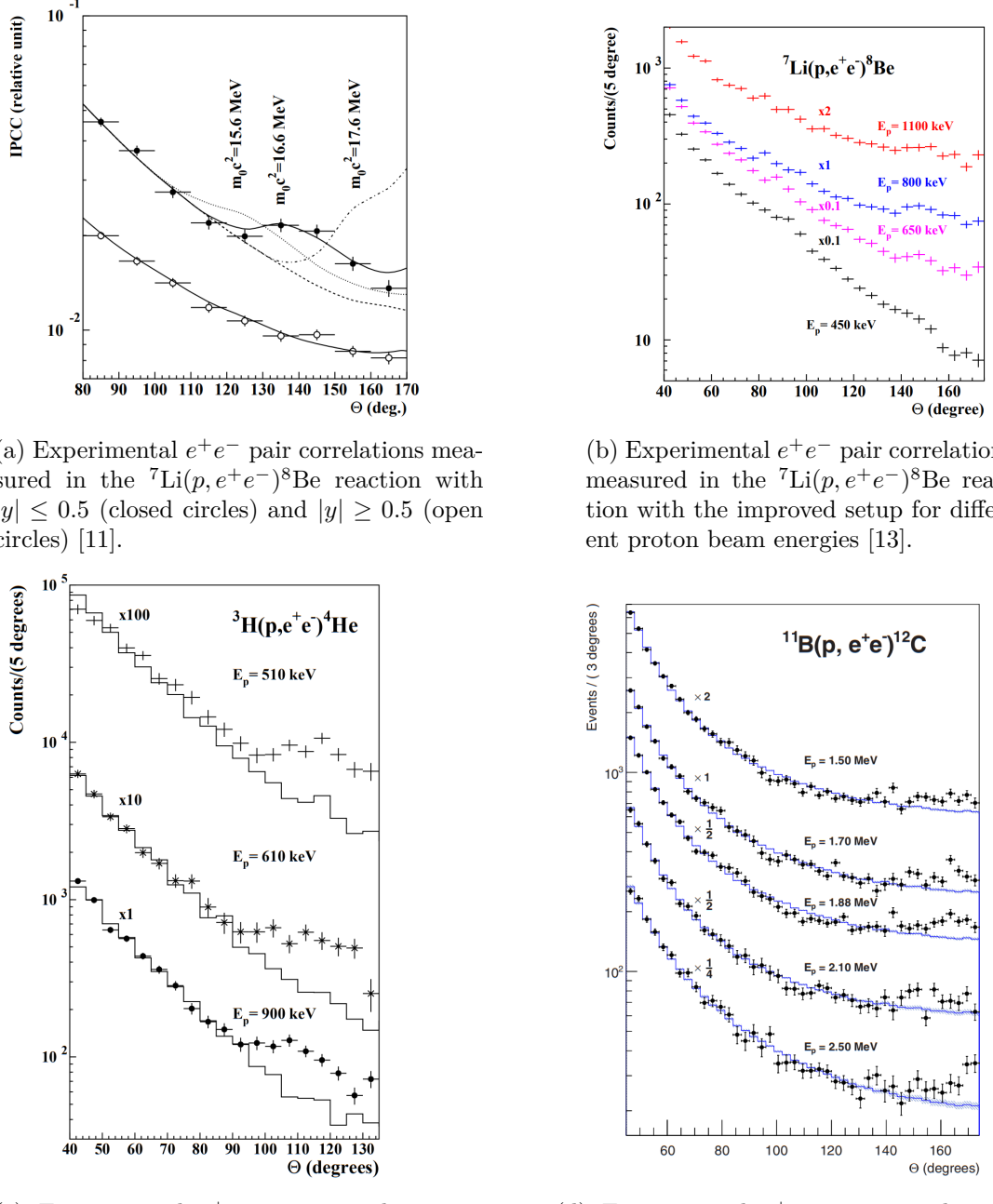


Figure 0.1: The ATOMKI anomalous IPC measured for different nuclei.



Figure 0.2: Results from the Hanoi spectrometer – angular e^+e^- pair correlations measured in the ${}^7\text{Li}(p, e^+e^-){}^8\text{Be}$ reaction at $E_p = 1225$ keV [21].

145 Two-arm e^+e^- spectrometer in Hanoi

146 The anomaly in ${}^8\text{Be}$ has been observed with a high ($> 4\sigma$ That's all they write
147 in their article.) confidence by a team at the Hanoi University of Sciences for
148 $E_p = 1225$ keV [21]. They built a two-arm spectrometer in collaboration with
149 ATOMKI and calibrated it using the 17.6 MeV M1 transition. The results are
150 shown in Fig. 0.2.

151 Collisions at Nuclotron in Dubna

152 At the Joint Institute for Nuclear Research in Dubna, signal in the form of en-
153 hanced structures in the $\gamma\gamma$ spectra at ~ 17 and ~ 38 MeV invariant masses for
154 $p + \text{C}$, $d + \text{C}$ and $d + \text{Cu}$ reactions at momenta 5.5, 2.75, and 3.83 GeV per nu-
155 cleon [22]. Monte Carlo simulations support the conclusion that the signals are
156 a consequence of a decay of unknown particles X17 and E38.

157 The MEG II (Muon Electron Gamma) experiment

158 Experiments using the ${}^7\text{Li}(p, e^+e^-){}^8\text{Be}$ reaction were carried out at the Paul
159 Scherrer Institute with the MEG II superconducting solenoid spectrometer [23].
160 Analysis of the data with $E_p = 1080$ keV exciting both of the resonances (beam
161 fully stopping in the target) found no significant evidence supporting the X17
162 hypothesis, results are shown in Fig. 0.3. An upper bound (at 90% confidence)
163 on the X17-to- γ branching ratio was set at $1.2 \cdot 10^{-5}$ for the 18.15 MeV state
164 (larger than the ratio $5.8 \cdot 10^{-6}$ obtained by ATOMKI in 2016). Could add their
165 90% C.L bounds figure also. Insufficient statistics – 6.2 % (1.5σ) p-value.

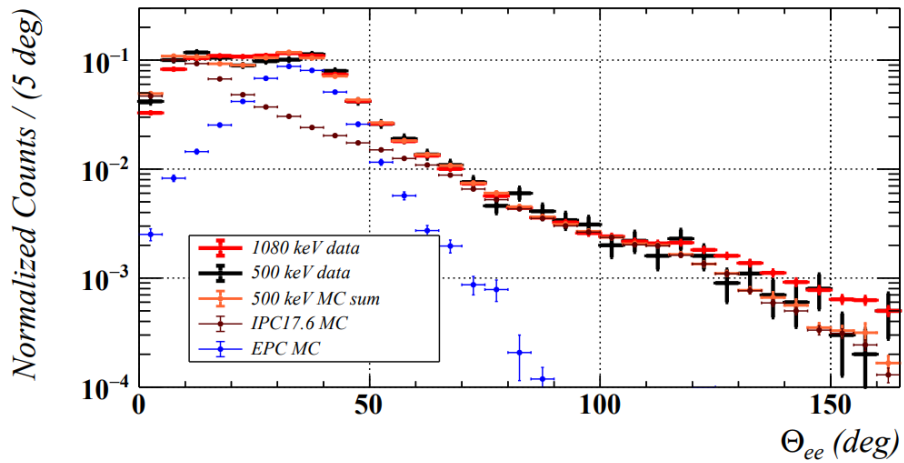


Figure 0.3: Results from the MEG II experiments – angular correlation of e^+e^- pairs with $E_{\text{sum}} \in [16, 20]$ MeV measured in the ${}^7\text{Li}(p, e^+e^-){}^8\text{Be}$ reaction with proton beam energies 500 and 1080 keV. The 500 keV dataset is fitted with Monte Carlo of both the IPC deexcitation and the EPC produced by gammas [23].

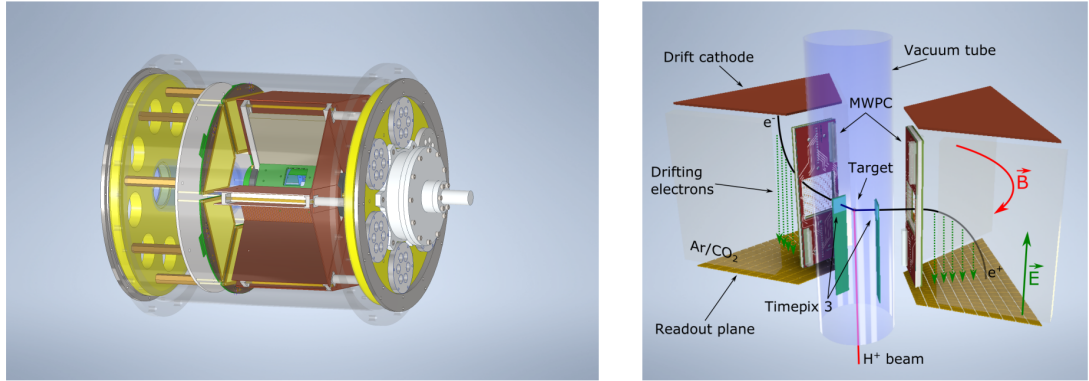


Figure 0.4: Schematics of the detector at the Van der Graaff facility at IEAP CTU (ref.).

166 0.2 X17 Project at IEAP CTU

167 The aim of the X17 project at the Van der Graaff facility of the Institute of
 168 Experimental and Applied Physics, Czech Technical University in Prague is to
 169 reproduce the results of the original ATOMKI experiments with ${}^7\text{Li}$ and ${}^3\text{H}$ tar-
 170 gets using an independent e^+e^- spectrometer. In order to effectively measure the
 171 anomaly, we need to reconstruct both the energy and the angular correlation of
 172 the e^+e^- pairs. The spectrometer will use three layers of detectors to achieve this
 173 – Timepix3 (TPX3) silicon pixel detector and Multi-Wire Proportional Cham-
 174 ber (MWPC) layers for the angle reconstruction and a Time Projection Cham-
 175 ber (TPC) layer for the energy reconstruction. The schematics of the prepared
 176 detector is in Fig. 0.4 Spectrometer CAD drawing (coordinates here or next chap-
 177 ter?). Cite some VdG paper, mention grant? Using https://cernbox.cern.ch/pdf-viewer/public/rf0oU1nqVLN3acZ/LuzH_submitted.pdf.

178
 179 The energy of e^+e^- pair produced in the reaction is given by the energy

available E_r in the reaction and can be distributed between them arbitrarily. Nonetheless in the decay of the hypothetical X17 particle, electron and positron should have similar energy and we can therefore use a cut $|y| \leq 0.5$ in the disparity parameter (defined in Equation 0.1 **it was already used in ATOMKI figure captions, that's why it is defined prior to this**). Interesting events should rarely have a particle with an energy below $E_r/4$ (roughly 4 MeV). Electrons with such low energies are scattered significantly by even a thin layer of relatively light material, for this reason the TPX3 layer will be inside of the vacuum tube and the tube will have a thinned aluminum segment or KaptonTM windows.

TPX3 can measure (in each $55 \times 55 \mu\text{m}$ pixel of its 256×256 grid) time-of-arrival (ToA) with 1.6 ns precision and time-over-threshold (ToT) which reflects the deposited energy. This potentially allows 3D tracking if we increase the chip thickness at the cost of increased scattering. The layer can reconstruct the reaction vertex and the angular correlation with high precision.

The layer of MWPCs with sensitive area $40 \times 38 \text{ mm}^2$ will be outside of the beam pipe. It will provide an extra point on the particle trajectory which can help with the estimation of the reaction vertex and improve the TPC performance by providing its entry point.

The TPCs that are the subject of this thesis, are in a magnetic field generated by permanent magnets positioned between them and provide 3D track reconstruction and subsequent momentum and particle identification (its charge, or even type based on its stopping power). They avoid radiative losses thanks to the low density and atomic number of the gas mixture. For the readout, triple Gas Electron Multiplier (GEM) will be used. The magnetic field layout in our TPCs is atypical – orthogonal to the electric field inside the chamber, this is why we call them Orthogonal Fields TPC (OFTPC). Further details about our OFTPCs are provided in section 1.4.

1. Time Projection Chamber

208 Using (2010 – a little old) <https://cds.cern.ch/record/1302071/files/CERN-PH-EP-2010-047.pdf>
209 A Time Projection Chamber (TPC) is a gaseous detector that uses the drift times
210 of ionization electrons produced by a charged particle in an (ideally uniform)
211 electric field to reconstruct the particle's 3D trajectory. The 2D projection is
212 measured by an amplification stage at the end of the drift volume. When placed
213 inside a magnetic field (typically parallel to the electric field), the momentum of
214 the incident particle can be inferred from the curvature of its trajectory. Particle
215 identification is also possible using the ionization energy loss inside the TPC (see
216 Fig. 1.1).

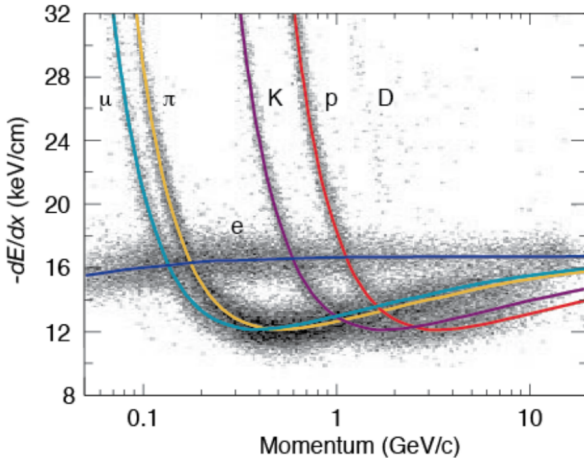


Figure 1.1: Particle identification in the PEP-4 TPC at SLAC based on the energy loss per distance $\frac{dE}{dx}$ in the 80:20 Ar:CH₄ filling at 8.5 atm pressure [24]. The reference doesn't point to the original PEP-4 article because this adapted version of the original picture that they used in the DUNE article looks better.

217 Large TPCs are sensitive to small distortions in the electric field (imperfec-
218 tions in the field cage, accumulation of positive ions in the gas volume) and to
219 $\mathbf{E} \times \mathbf{B}$ effects on the drift velocity (see Eq. (1.1) below). Diffusion of the drifting
220 electrons deteriorates the spacial resolution significantly, but it can be reduced
221 up to ~ 10 times by a strong $\mathbf{B} \parallel \mathbf{E}$ field (see Eq. (1.8)).

222 In neutrino and other rare-event experiments, large (up to 600 tons) Liquid
223 Argon TPCs (LArTPCs) are used for particle identification and calorimetry. The
224 ionization electrons can be drifted for many meters with a small diffusion. Negative
225 ions?

226 1.1 Charge transport in gases

227 When a charged particle crosses the volume of a TPC, it loses energy by exci-
228 tation and ionization of the detector gas (how much – from $dE/dx +$ density
229 → footnote?). Most ionizing collision produce a single ionization electron, some-
230 times a few secondary electrons are produced near the collision vertex, creating
231 a cluster. In rare cases, the ionization electron has energy large enough to create

232 a measurable track, such an electron is called a δ -electron (terminology, just like
233 bellow – technically it's a (primary) ionization electron causing other (secondary)
234 ionization).

235 After their release, the ionization electrons are separated from positive ions
236 by the electric field and they both drift and diffuse in opposite directions towards
237 the electrodes. The charges are accelerated (different word?) by the electric field
238 inside the chamber, and they lose speed by colliding with the gas particles, quickly
239 reaching a constant (for a given field \mathbf{E}, \mathbf{B}) mean drift velocity. The electrons can
240 be absorbed by electronegative impurities, such as halides, O_2 , and H_2O .

241 In mixtures with a noble gas component, if the excitation energy of the noble
242 gas is higher than the ionization potential of an admixture, more free electrons can
243 be produced through collisions of the gas particles (so-called Penning transfer)
244 and through absorption of emitted photons.

245 If the electric field is strong enough, the electrons can cause further ion-
246 ization and excitation of the gas, leading to the development of a Townsend
247 avalanche (ref).

248 1.1.1 Drift

249 In many gases (called "hot", e.g., Ar or CH_4), the drift velocity is much greater
250 than that of their thermal motion thanks to a high proportion of elastic collisions.
251 On the other hand, "cold" gases like CO_2 have a higher proportion of inelastic
252 collisions (e.g., thanks to the excitation of rotational and vibrational states) and
253 therefore much lower (value? magnitude (implied)?). Or maybe it
254 is not so simple, because slowing down the electrons inelastically into a certain
255 minimum of elastic scattering cross-section increases drift velocity? In case of
256 $\text{Ar}+\text{CO}_2$ this is clearly not the case for low electric fields, so maybe irrelevant
257 here (or is the effect opposite for small additions?).

258 The ions produced by the ionization lose a significant portion of their energy
259 during each collision since their mass is close to the mass of the gas particles (see
260 the source material – average energy loss during collision $\Delta E = \frac{2m_i M}{(m_i + M)^2}$, this
261 way it's more accurate). This, together with their large collision cross section,
262 makes their drift velocity much smaller (about three orders of magnitude) and
263 their energy is close to thermal. Since their momenta are not randomized to such
264 an extent during collisions, their diffusion is smaller (move this to the diffusion
265 subsection, reformulate).

266 The drift is also influenced by the magnetic field. Langevin derived a good
267 approximation for the drift velocity vector:

$$\mathbf{v}_d = \left(\frac{\mathbf{E}}{\|\mathbf{E}\|} + \omega\tau \frac{\mathbf{E} \times \mathbf{B}}{\|\mathbf{E}\| \|\mathbf{B}\|} + \omega^2\tau^2 \frac{\mathbf{E} \cdot \mathbf{B}}{\|\mathbf{E}\| \|\mathbf{B}\|} \cdot \frac{\mathbf{B}}{\|\mathbf{B}\|} \right) \frac{q\tau}{m(1 + \omega^2\tau^2)} \|\mathbf{E}\|, \quad (1.1)$$

268 where q is the charge of the particle, m is its mass, τ is the mean time between
269 collisions and $\omega = \frac{q}{m} \|\mathbf{B}\|$ is the Larmor frequency. For orthogonal fields $\mathbf{E} \perp \mathbf{B}$,
270 it can be shown that the magnetic field bends the direction of the drift by the
271 so-called Lorentz angle:

$$\tan \psi = -\omega\tau. \quad (1.2)$$

272 The drift of ions is only negligibly influenced by the magnetic field ($\omega\tau \sim 10^{-4}$
273 is small due to the low drift velocity – better (?) because it takes τ into account

²⁷⁴ and differs only by E/B ratio (if the magnetic contribution to the magnitude is
²⁷⁵ small)). In a standard TPC, \mathbf{E} is parallel to \mathbf{B} and the influence of the magnetic
²⁷⁶ field on the drift is minimal. Without magnetic field, we can write

$$\mathbf{v}_d = \frac{q\tau}{m} \mathbf{E} = \mu \mathbf{E}, \quad (1.3)$$

²⁷⁷ where μ is called charge mobility.

²⁷⁸ 1.1.2 Diffusion

²⁷⁹ All of the theory is from the same source mentioned at the beginning. None of the
²⁸⁰ simulations explicitly depend on this. Due to collisions, a cloud of electrons or
²⁸¹ ions originating from the same point will show a Gaussian density distribution at
²⁸² time t while drifting in the electric field $\mathbf{E} = (0, 0, E_z)$ along the z -coordinate (²⁸³ coordinates defined by the electric field):

$$\rho(x, y, z, t) = (4\pi Dt)^{-\frac{3}{2}} \exp\left(-\frac{x^2 + y^2 + (z - v_d t)^2}{4Dt}\right), \quad (1.4)$$

²⁸⁴ where the diffusion coefficient D can be expressed as

$$D = \frac{\lambda^2}{3\tau} = \frac{\lambda v_d}{3} = \frac{v_d^2 \tau}{3} = \frac{2\varepsilon\tau}{3m}, \quad (1.5)$$

²⁸⁵ where λ is the mean free path and ε the mean kinetic energy. The lateral diffusion
²⁸⁶ width σ_x after a drift distance L can be expressed as

$$\sigma_x^2 = 2Dt = \frac{4\varepsilon L}{3qE_z}. \quad (1.6)$$

²⁸⁷ The minimal diffusion width is given by the lowest possible energy of the particles
²⁸⁸ $\varepsilon_{\text{th}} = \frac{3}{2}kT$ (corresponding to thermal motion):

$$\sigma_{x, \text{min}}^2 = \frac{2kTL}{qE}. \quad (1.7)$$

²⁸⁹ For electrons in "cold gases" (e.g., Ar/CO₂ mixture), the diffusion approaches
²⁹⁰ this limit up to a certain field intensity (~100 V/cm at 1 atm pressure)¹. In
²⁹¹ reality, the transversal diffusion of electrons can differ significantly from their
²⁹² longitudinal diffusion and simulations are necessary to get a precise result.

²⁹³ In most TPCs, the transversal (but not the longitudinal) diffusion is reduced
²⁹⁴ by the magnetic field, since it is parallel to the electric field and curves the dif-
²⁹⁵ fusing electrons around their mean trajectory:

$$\frac{D_T(B)}{D_T(0)} = \frac{1}{C + \omega^2 \tau_2^2}, \quad (1.8)$$

²⁹⁶ where C and τ_2 are parameters dependent on the gas used. At low intensity of
²⁹⁷ the magnetic field, we can use an approximation $C \approx 1$ and $\tau_2 \approx \tau$.

¹For us $\sigma_{x, \text{min}} = 0.45$ mm, quite close to the actual diffusion 0.5-0.7 mm – details of the calculation.

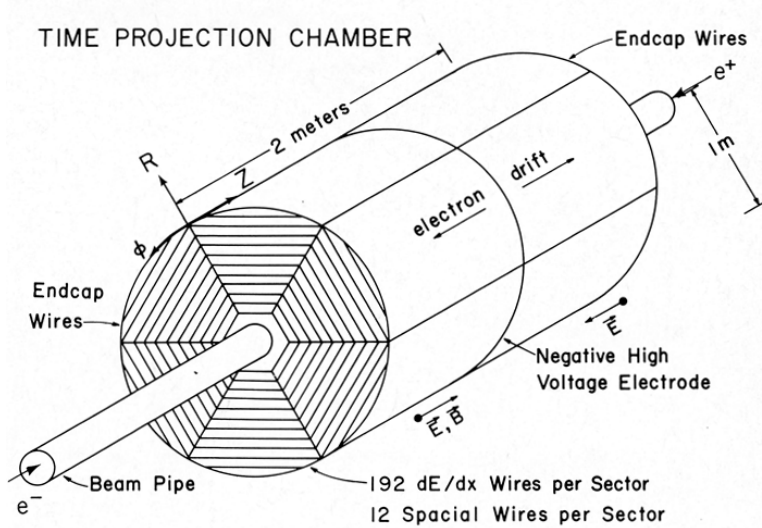


Figure 1.2: Schematic view of the PEP-4 TPC [25]. A charged particle produced in a collision in the beam pipe creates a spiral ionization track in the magnetic field. The central cathode then accelerates ionization electrons towards the endcap anode wires where they are multiplied and read out.

298 1.2 Examples of TPCs

299 1.2.1 The original TPC at PEP-4 at SLAC

300 The original TPC used in the PEP-4 experiment at SLAC in the 1980s (Fig. 1.2)
 301 was a 2×2 m cylinder with a central cathode that produced a strong electric field,
 302 making the ionization electrons drift towards one of the endcaps. The readout
 303 consisted of MWPCs, where electrons are accelerated towards the anode wires
 304 enough to further ionize the gas and cause an avalanche.

305 1.2.2 The ALICE TPC

306 1.2.3 The CERES/NA45 radial drift TPC

307 CERES/NA45 – very inhomogeneous magnetic field. They used look-up tables for
 308 reconstruction, which they calculated by integrating the Langevin drift velocity
 309 equation with Runge-Kutta.

310 From [26]:

311 10.2 Coordinate transformation The detector specific hit coordinates (pad, time,
 312 plane) are transformed to spatial coordinates (x, y, z) via look-up tables. The
 313 transformation contains the information about the transport process of the charged
 314 clusters in the electric and magnetic fields inside the TPC. The look-up tables
 315 are calculated using a Runge-Kutta method [39] that calculates the drift trajec-
 316 tory using in each point the drift velocity vector (Eq. 3), starting at the cathode
 317 plane. The drift between the cathode plane and the pad plane is absorbed in a
 318 φ -dependent time offset due the fact that each Front-End Electronic (FEE) chan-
 319 nel had a slightly different capacitance. The difference between the MAGBOLTZ
 320 Monte Carlo drift [19] and the actual drift velocity vector is accounted for with a

321 z- and r(E)-dependent correction for the drift velocity component parallel to the
322 electric field and the one parallel to $E \times B$

323 1.3 Readout

324 1.3.1 Multi-Wire Proportional Chamber

325 In most TPCs operated in experiments, Multi-Wire Proportional Chamber (MWPC)¶
326 was used for the readout. The electrons enter the chamber through a cathode
327 grid and get accelerated by a strong electric field towards the parallel, thin an-
328 ode wires and create an avalanche, multiplying the signal. The trajectory can be
329 reconstructed from the drift time and two coordinates measured using
330 a) two segmented cathodes (wires or strips) rotated by 90° or
331 b) the ratio of charge collected on two sides of the hit resistive wires.
332 For high counting rates, the positive ions from the avalanches accumulate, cre-
333 ating a space charge that distorts the electric field. This can be solved by using
334 a gating grid near the readout plane to collect these ions at the cost of introducing
335 a dead time in the detector. [Add some figure.](#)

336 1.3.2 Micro-Pattern Gaseous Detectors

337 In order to avoid MWPC limitations (e.g., diffusion, wire $E \times B$ effect, space
338 charge effects), a family of Micro-Pattern Gaseous Detector (MPGD) technologies
339 are being developed. The readouts can reach higher spatial resolution (down to
340 30 μm) with faster response time (ns range) and much higher rate capability.

341 Gas Electron Multiplier

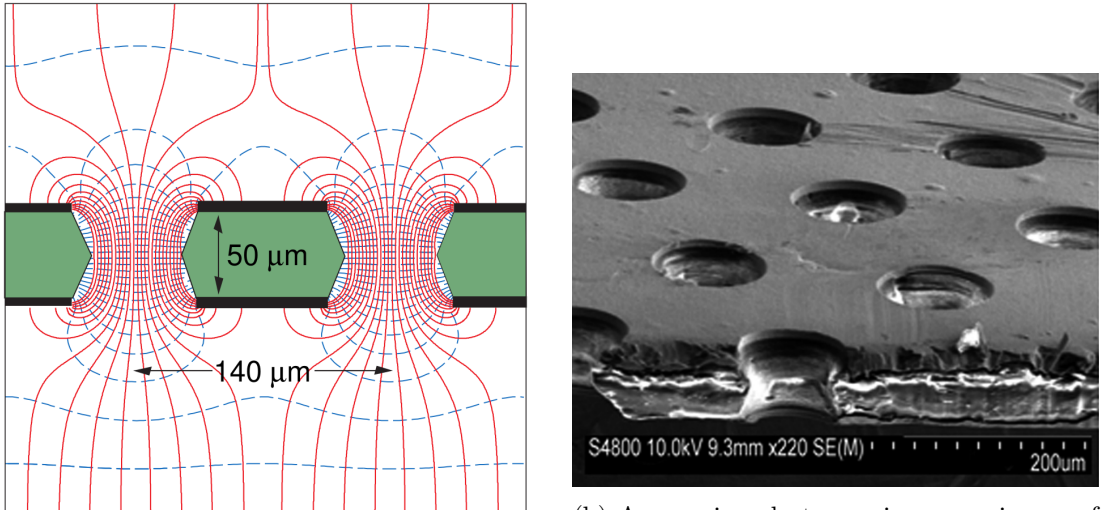
342 A Gas Electron Multiplier (GEM) is a thin metal-coated polyimide sheet with
343 a dense pattern of small, chemically etched holes (Fig. 1.3). The amplification
344 is achieved by applying voltage across the metal layers and placing the foil be-
345 tween two moderate uniform electric fields. This creates a strong electric field
346 inside the holes that accelerates the incoming electrons and causes avalanches
347 (see Fig. 1.4). Some charges may land on the dielectric surfaces due to diffusion,
348 modifying the field and affecting gain.

349 Double or triple stacks of GEMs are usually used to create a sufficient gain
350 while maintaining stability (reducing discharges). From the last foil, the electrons
351 drift to a segmented anode where the signal is read. The ion backflow is reduced
352 compared to MWPC.

353 A cheaper alternative (especially for large area coverage) is a THick GEM
354 (THGEM) with a ~10-fold upscaling of geometrical parameters. It can be made
355 by mechanically drilling holes into a standard Printed Circuit Board (PCB) and
356 creating a circular rim around the holes by etching the metal coating.

357 Micromegas

358 In a MICRO-MEsh GAseous Structure (Micromegas) ([in sources I viewed it is not](#)
359 [capitalized](#)) electrons pass through a fine mesh (made out of very thin wires) into
360 a narrow amplification gap where they are multiplied in the high field and read



(a) A schematic view of a GEM cell with its typical dimensions, electric field lines (red), and equipotentials (blue) [27].

(b) A scanning electron microscope image of a GEM foil [28].

Figure 1.3: Gas Electron Multiplier (GEM).

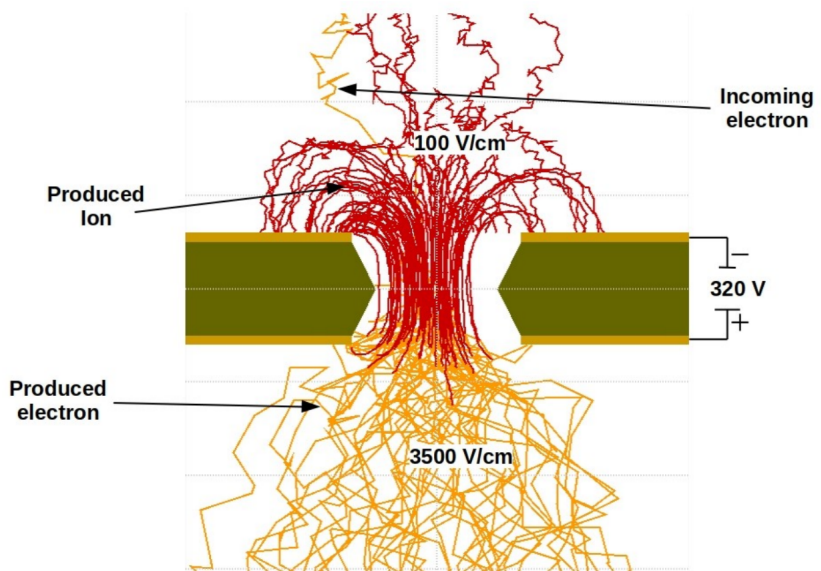
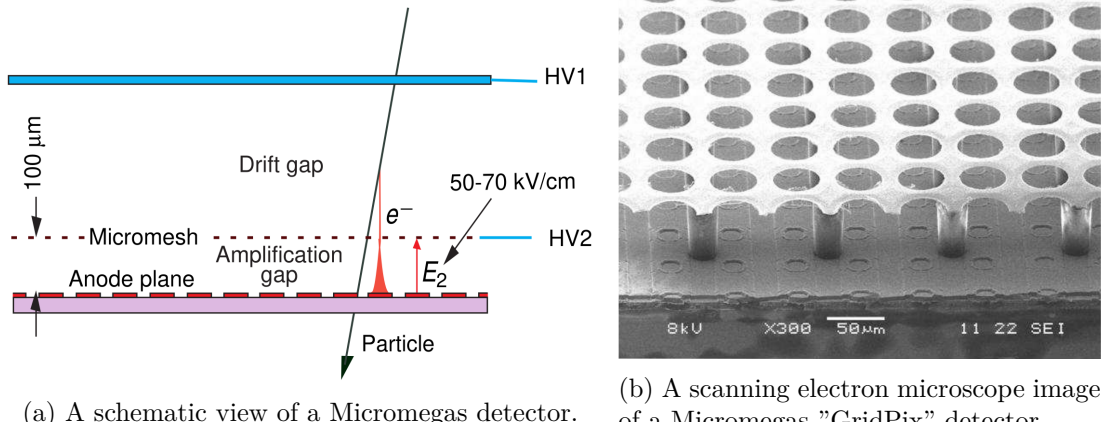


Figure 1.4: Garfield simulation of an avalanche in a GEM hole [29]. An incoming electron (orange) is accelerated in the strong electric field of the GEM and causes further ionization multiplying the number of free electrons (orange). Most of the produced cations (red) are captured by the GEM cathode.



(a) A schematic view of a Micromegas detector.

(b) A scanning electron microscope image of a Micromegas "GridPix" detector.

Figure 1.5: MICRO-MEsh GAseous Structure (Micromegas) [27].

as a signal on the segmented anode (Fig. 1.5a). Very high field ($30-80 \text{ kV/cm}^2$) is necessary to achieve sufficient gain. Ion backflow is heavily suppressed by the mesh.

A Timepix chip (a high granularity pixel detector) can be used for the readout anode to achieve the best spatial resolution, making an integrated readout called GridPix (Fig. 1.5b). Thanks to the high spatial resolution, it is possible to distinguish individual electron clusters, which enables a new method of particle identification.

Other MPGDs

A Resistive Plate WELL (RPWELL) consists of a THGEM with only the top side metal-coated, mounted on a resistive film deposited on a thin isolating sheet (which is read out similarly to a Resistive Plate Chamber (RPC)). Due to the higher field in the closed holes of the THGEM, a higher gain can be reached for the same voltage. A Micro-RWELL (μ -RWELL) is a similar architecture with ~ 7 times smaller pitch (distance between holes). These options provide a better spark resistance and could allow to cover large areas for a lower cost.

A Micro-Pixel Gas Chamber (μ -PIC) is a PCB with anode strips on one side and orthogonal cathode strips on the other. The cathode has a resistive coating and a regular pattern of uncoated regions with anode "dots" penetrating the PCB at the centers.

1.4 Orthogonal Fields TPC at IEAP CTU

At IEAP CTU, we are going to use six identical atypical TPCs with inhomogeneous toroidal magnetic field **orthogonal** to the electric field (details below), hereafter referred to as Orthogonal Fields TPC (OFTPC). It has the shape of isosceles trapezoidal prism 16 centimeters high with triple-GEM readout on one of its bases. Dimensions of the OFTPC are discussed in detail in section 1.4.2 below. Throughout this thesis, we assume a uniform electric field along the z axis with $E_z = -400 \text{ V/cm}$. Isn't the field affected by the MWPCs? Eventually a simulation will be needed. Measured particles enter the OFTPC through a window

390 after crossing the MWPC. Gas mixture used in the detector (70/30) and its effect
391 – some graph with the mixture, reasons for the choice. Add a figure of the real
392 TPC. More about the design choices.

393 1.4.1 Motivation and Associated Challenges

394 The reasons for the unusual field layout are mostly cost related:

- 395 a) we use permanent magnets instead of a solenoid and parallel fields are
396 difficult to accomplish this way,
- 397 b) granularity of the TPC readout is limited in order to fit one SAMPA/SRS
398 hybrid in each sector – parallel fields would bend the trajectories parallel
399 to the readout requiring more pads and different architecture.

400 In this thesis, we will show that such a setup can reach a similar energy resolution
401 as common cylindrical TPCs while reducing the overall cost.

402 The layout introduces two complications to the track reconstruction – the
403 trajectory in inhomogeneous field is not circular and the drift is distorted by the
404 magnetic field as shown in the Equation 1.1(in our case $\omega\tau \approx 0.08$ for 0.3 T
405 assuming $\mu \approx 0.25 \text{ T}^{-1}$, varies inside the detector). We will deal with these
406 effects in the upcoming chapters.

407 The diffusion in such setup is larger since parallel orientation reduces diffusion
408 by curling the electrons in the x - y direction (see Equation 1.8), but for our
409 relatively weak magnetic field and short drift distance, the difference is negligible.

410 1.4.2 Coordinate Systems and Dimensions

411 In order to describe events in our detector, we use three distinct spaces: the de-
412 tector space \mathcal{D} , the readout space \mathcal{R} and the pad space \mathcal{P} (different spaces that
413 describe different things and each has their own coordinate system, so maybe
414 rename the section somehow?). Each space is later used to represent ionization
415 electrons at different stages of the detection process: their creation in the gas,
416 their final position when hitting the readout plane, and finally their representation
417 in the discrete pad space.

418 Detector Space

419 The detector space \mathcal{D} represents the physical space of our detector. We de-
420 scribe it using Cartesian coordinates (x, y, z) . The z -axis is the detector's axis of
421 symmetry, with its negative direction aligned with the proton beam. The origin
422 $(0, 0, 0)$ is located at the center of the irradiated target. The positive x -axis passes
423 through the center of one the OFTPCs along the intersection of its two planes
424 of symmetry. The y -axis is then chosen to maintain a right-handed coordinate
425 system.

426 Since the detector has a hexagonal symmetry, we use only one of its sectors
427 in this work – the first sector $\mathcal{D}_1 \subset \mathcal{D}$ which is defined by the condition:

$$(x, y, z) \in \mathcal{D}_1 \Leftrightarrow |y| \leq x \tan \frac{\pi}{6}. \quad (1.9)$$

428 Simulations in this sector can be applied to all sectors by rotating the coordinates
429 accordingly. The volume of the OFTPC in this sector, which has the shape of

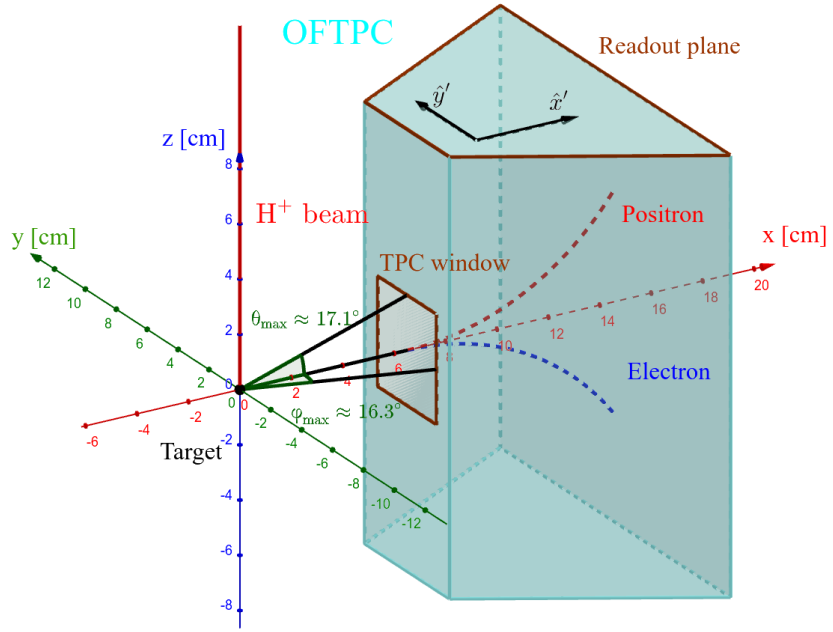


Figure 1.6: Schematics of the first sector OFTPC with detector space coordinates.

430 a trapezoidal prism, has these boundaries:

$$x \in [x_{\min}, x_{\max}] = [6.51, 14.61] \text{ cm}, \quad (1.10)$$

$$z \in [z_{\min}, z_{\max}] = [-8, 8] \text{ cm}, \quad (1.11)$$

$$y_{\max}(x_{\min}) = -y_{\min}(x_{\min}) = 2.75 \text{ cm}, \quad (1.12)$$

$$y_{\max}(x_{\max}) = -y_{\min}(x_{\max}) = 7.45 \text{ cm}, \quad (1.13)$$

431 where $y_{\max}(x)$ is the maximal value of the y -coordinate for a given x . The read-
432 out is located at $z = 8$ cm; for some purposes, we also define the distance to
433 the readout $d_r = 8$ cm – z as an alternative to the z -coordinate. Keeping this
434 paragraph as it is because the OFTPC volume is distinct from the first sector
435 and some parts of this thesis use the space beyond this volume. The OFTPC
436 window has width 3.8 cm and height 4.0 cm.

437 We also use spherical coordinates (r, θ, φ) with the elevation angle θ measured
438 relative to the xy plane. Angles θ and φ are useful when describing the direction
439 of e^+/e^- tracks. Their maximal values considered for the initial direction in
440 simulations are $\theta_{\max} \approx 17.1^\circ$ and $\varphi_{\max} \approx 16.3^\circ$ as shown in Fig. 1.6.

441 Readout Space

442 The readout space \mathcal{R} represents the drift time and final positions of ionization
443 electrons as measured by an ideal continuous readout. We describe it using
444 coordinates (x', y', t) , where x' and y' correspond to the detector coordinates at
445 the readout plane ($z = 8$ cm).

446 Currently not entirely sure how to put this into a figure since only x' and
447 y' correspond to the detector coordinates, it will make more sense when
448 visualizing the map. The drift time t is approximately proportional to d_r .

449 **Pad Space**

450 The pad space \mathcal{P} represents the time bin and pad number of ionization electrons
 451 as measured by an ideal discrete readout:

$$\mathcal{P} = \{(n_{\text{pad}}, n_t) \in \mathbb{N}^2 \mid n_{\text{pad}} \leq 128\}. \quad (1.14)$$

452 **Rewrite to reflect this:** Technically both values can be zero as defined in
 453 the code (max channel 127). It is not really a subspace of \mathcal{R} but there is a
 454 mapping from \mathcal{R} to \mathcal{P} . It is a discretization of a part of \mathcal{R} , the mapping can be
 455 adjusted depending on the simulation. If we assume uniform electric field there
 456 will be gaps, we don't use gaps in the reconstruction since the electrons should
 457 be pulled towards the pads.

458 The readout of the OFTPC will consist (is the design final?) of 128 rectangular
 459 pads arranged in a staggered pattern. Parameters of the pad layout are
 460 shown in Fig. 1.7. The bottom left corner of n -th pad has coordinates $(x_{1,n}, y_{1,n})$,
 461 the top right $(x_{2,n}, y_{2,n})$ and its center has coordinates $(x_{c,n}, y_{c,n})$. The gap be-
 462 between neighboring pads is $g = 0.08$ cm. Time will be read out in discrete bins of
 463 size $t_{\text{bin}} = 100$ ns (details?). Could also describe pad-related functions.

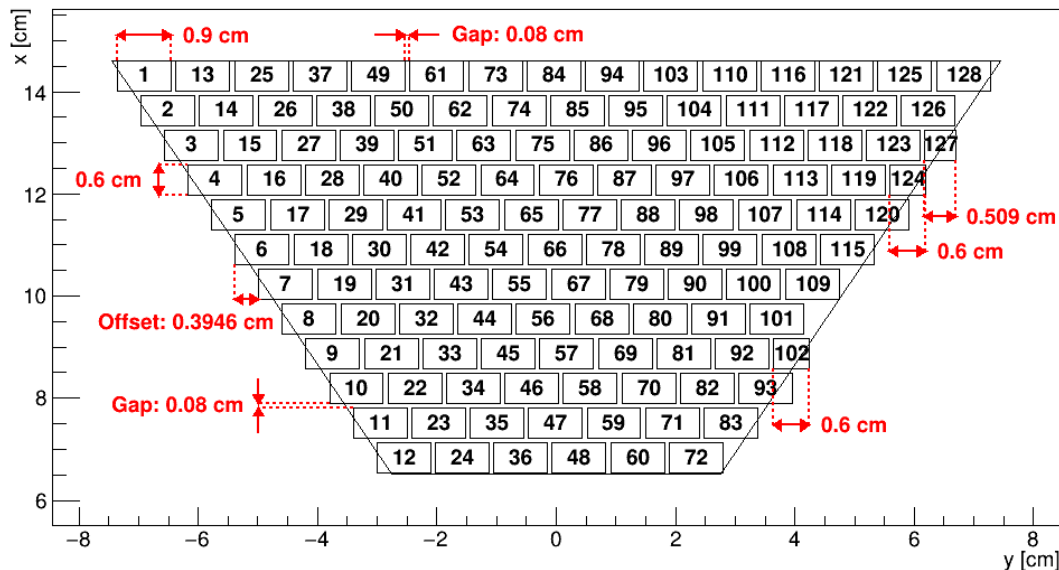
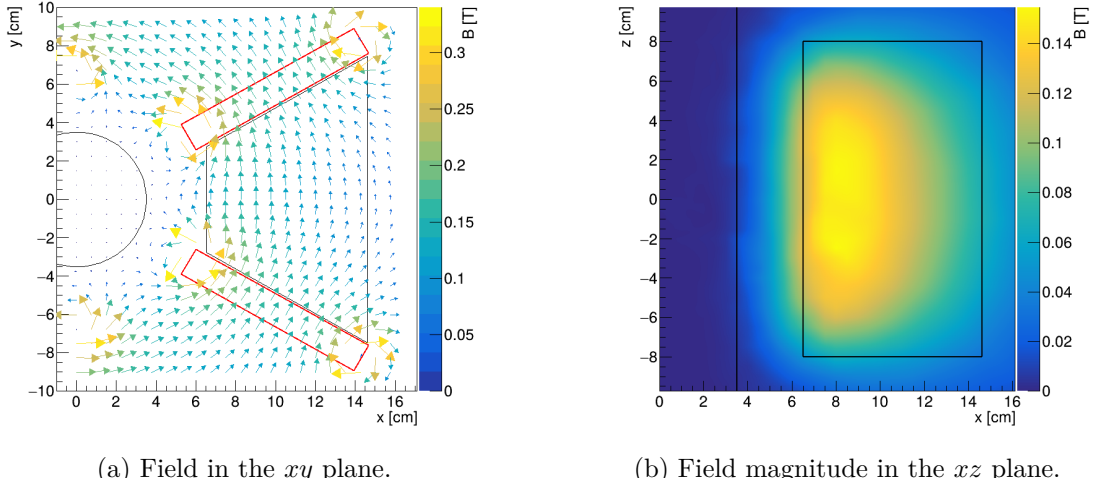


Figure 1.7: Pad layout of the OFTPC and its parameters. Pads 102, 124 and 127 are irregular, the rest has the same dimensions.

464 **1.4.3 Magnetic Field Simulation**

465 The magnetic field inside our detector is produced by six permanent magnets. It
 466 was simulated using Ansys Maxwell (citation) which gives us values on a regular
 467 grid. More details, vacuum tube, magnets (homogeneous?, density?). Visualiza-
 468 tion of the magnetic field is shown in Fig. 1.8. Whenever we need to work with
 469 values outside this grid, we use trilinear interpolation described below.



(a) Field in the xy plane.

(b) Field magnitude in the xz plane.

Figure 1.8: Magnetic field simulation results. The OFTPC volume and the vacuum tube are marked with black lines, the magnets are marked with red lines. **The coordinates of the magnets from the CAD drawing seem to be 9/10 of the ones from the magnetic simulation (confirm and fix).**

470 Trilinear Interpolation

471 Trilinear interpolation is a 3D generalization of linear interpolation². It can be
 472 used to interpolate a function whose values are known on a regular grid with
 473 rectangular prism cells. We use this simple method for interpolating the magnetic
 474 field, and it is later used in Section 3.2.1 to interpolate the Ionization Electron
 475 Map, a key component of our track reconstruction algorithm. In both cases, we
 476 use a regular cubic grid (apparently it is also called a [Cartesian grid](#)).

477 Let us consider a cell of our regular grid (a cube) with an edge of length a
 478 containing the point $\mathbf{C} = (x, y, z)$ where we want to interpolate a function
 479 $f: \mathbb{R}^3 \rightarrow \mathbb{R}$. We know the values of this function at the vertices of the cell $\mathbf{C}_{ijk} =$
 480 $= (x_0 + ia, y_0 + ja, z_0 + ka)$, where $\mathbf{C}_{000} = (x_0, y_0, z_0)$ is the origin of the cell ([is](#)
 481 [that clear?](#)), and $i, j, k \in \{0, 1\}$ are indices. We also define the points $\mathbf{C}_{ij} =$
 482 $= (x, y_0 + ia, z_0 + ja)$ and $\mathbf{C}_i = (x, y, z_0 + ia)$. Then the interpolated value $\hat{f}(\mathbf{C})$
 483 can be calculated as a composition of three linear interpolations (see Fig. 1.9):

$$\hat{f}(\mathbf{C}_{ij}) = (1 - x_d) f(\mathbf{C}_{0ij}) + x_d f(\mathbf{C}_{1ij}), \quad (1.15)$$

$$\hat{f}(\mathbf{C}_i) = (1 - y_d) \hat{f}(\mathbf{C}_{0i}) + y_d \hat{f}(\mathbf{C}_{1i}), \quad (1.16)$$

$$\hat{f}(\mathbf{C}) = (1 - z_d) \hat{f}(\mathbf{C}_0) + z_d \hat{f}(\mathbf{C}_1), \quad (1.17)$$

484 where x_d , y_d , and z_d are given as follows:

$$x_d = \frac{x - x_0}{a}, \quad y_d = \frac{y - y_0}{a}, \quad z_d = \frac{z - z_0}{a}. \quad (1.18)$$

²Linear interpolation in point $x \in (x_1, x_2)$ of a function $f: \mathbb{R} \rightarrow \mathbb{R}$ known in points $x_1 < x_2$ is the convex combination $\hat{f}(x) = (1 - x_d)f(x_1) + x_d f(x_2)$, where $x_d = \frac{x - x_1}{x_2 - x_1} \in (0, 1)$.

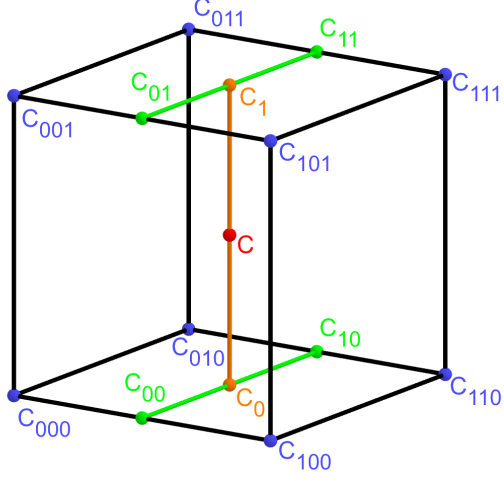


Figure 1.9: Visualization of trilinear interpolation as a composition of linear interpolations (inspired by [30]). We want to interpolate the value in the red point \mathbf{C} . First we interpolate between the four pairs of blue points sharing the last two indices along the x -axis (Eq. 1.15), then between the two pairs of the resulting green points along the y -axis (Eq. 1.16) and finally between the two resulting orange points along the z -axis to get the final red value (Eq. 1.17).

485 We can also write

$$\hat{f}(\mathbf{C}) = \sum_{i,j,k \in \{0,1\}} t_x^i t_y^j t_z^k f(\mathbf{C}_{ijk}), \quad (1.19)$$

$$t_\alpha \stackrel{\text{def}}{=} \begin{pmatrix} t_\alpha^0 \\ t_\alpha^1 \end{pmatrix} = \begin{pmatrix} 1 - \alpha_d \\ \alpha_d \end{pmatrix}, \quad (1.20)$$

486 where $\alpha \in \{x, y, z\}$ is an index. This gives a nice geometric interpretation to the
 487 trilinear interpolation as shown in Fig. 1.10. From this form and the figure, it is
 488 apparent that the final interpolated value does not depend on the order of axes
 489 along which we perform linear interpolations (see Fig. 1.9). Furthermore, we can
 490 write $\hat{f}(\mathbf{C})$ as a polynomial:

$$\hat{f}(\mathbf{C}) = \sum_{\alpha, \beta, \gamma \in \{0,1\}} \sum_{i=0}^{\alpha} \sum_{j=0}^{\beta} \sum_{k=0}^{\gamma} (-1)^{(\alpha-i)+(\beta-j)+(\gamma-k)} f(\mathbf{C}_{ijk}) x_d^\alpha y_d^\beta z_d^\gamma. \quad (1.21)$$

491 We take advantage of this form when generalizing trilinear interpolation to irreg-
 492 ular grid in section 3.2.2.

493 Maybe a citation here, although I am not sure it is necessary since it could
 494 be considered common knowledge. The last two equations are my own (but I'm
 495 not sure that's worth mentioning unless there's a citation).

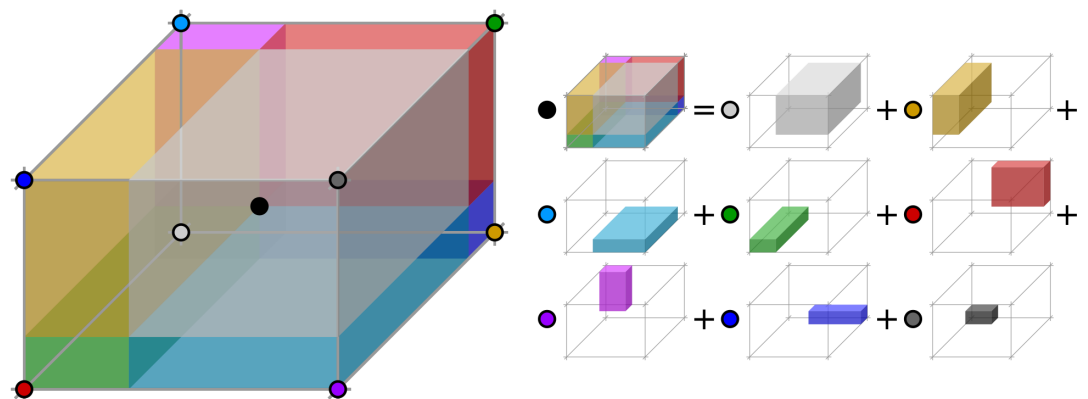


Figure 1.10: Geometric interpretation of trilinear interpolation as expressed in Equation 1.19. The colored dots represent the values in given points and the colored boxes represent the volume in the opposite corner by which the corresponding values are multiplied. The black dot represents the interpolated value which is multiplied by the entire volume [31].

2. Track Simulation

In order to develop and test the reconstruction algorithm, electron and positron tracks are simulated inside the first detector sector \mathcal{D}_1 (see Section 1.4.2) with different initial parameters (origin, initial direction and kinetic energy). Two approaches are currently used to simulate tracks, each of them for different purpose.

The **Microscopic Simulation** uses the Garfield++ toolkit [1]. Within this toolkit:

- a) Magboltz, since it is mentioned later. Or maybe just class MediumMagboltz with the collision rates?
- b) the High Energy Electro-Dynamics (HEED) program [32] is used to simulate the primary particle,
- c) the class *AvalancheMicroscopic* to simulate the drift of secondary electrons created by ionization in the gas.

This is the most precise and time-consuming simulation used; our current goal is to be able to successfully reconstruct its results and determine our best-case energy resolution.

The **Runge-Kutta Simulation** uses the 4th order Runge-Kutta numerical integration (add citation for Runge-Kutta) to simulate the trajectory of the primary particle in the electromagnetic field inside the detector. It is relatively fast since it does not simulate the secondary particles. It is used as part of our reconstruction algorithm and for testing some parts of the reconstruction.

All of these simulations require the knowledge of the electromagnetic field (both **E** and **B**) inside the detector. A uniform electric field of $400 \text{ V}\cdot\text{cm}^{-1}$ is assumed. The magnetic field was simulated in Maxwell (see Section 1.4.3). add citation

Single track in positive x direction or initial parameter randomization. Importance of gas composition, used gas compositions.

2.1 Microscopic Simulation

The microscopic simulation, the most detailed simulation used in this work, is performed using the Garfield++ toolkit [1].

The electron transport properties are simulated using the program Magboltz (add citation), (details?). Two different gas mixtures were compared – 90:10 and 70:30 Ar:CO₂. The second mixture will be used in our detector (this was probably known a priori, but the first tests that I started with used 90/10, so maybe just note that the results justify the fact so far). The temperature is set to 20 °C, the pressure is atmospheric.

The primary track is simulated using the program HEED, which is an implementation of the photo-absorption ionization model [32] (see the reference, moved it to the end of sentence). This program provides the parameters of ionizing collisions. HEED can also be used to simulate the transport of delta electrons; we do not account for these in the current simulation (but plan to include them in the future – maybe mention only in the conclusion/future section). The photons created in the atomic relaxation cascade (fluorescence reabsorption, related to the spread of avalanches in GM det.?) are also not simulated.

540 Finally, we use the microscopic tracking provided by the class *AvalancheMicroscopic* in Garfield++ to simulate the drift of the ionization electrons. Each
 541 electron is followed from collision to collision using the equation of motion and
 542 the collision rates calculated by Magboltz (how fast is this? maybe it slows down
 543 the simulation when spreading it across multiple jobs?).

544 Add more detailed and better description of HEED, and microscopic tracking
 545 (each their own subsection?). Could also mention Monte Carlo (requires gas file
 546 generation - Magboltz) and Runge-Kutta simulation implemented in Garfield,
 547 why we don't use them (another subsection? rename the section to Garfield++
 548 simulation and mention all relevant parts?).

550 2.1.1 First testing track

551 The first electron track simulated for testing purposes was chosen to have a special
 552 set of parameters:

- 553 • the starting point of the track is the origin of the coordinate system,
- 554 • the initial direction is along the positive x -axis,
- 555 • the momentum is 8 MeV/c (the kinetic energy is 7.505 MeV).

556 Such a track moves in the XZ plane in the toroidal magnetic field of the detector,
 557 because the particle's velocity vector is always perpendicular to the field. At first,
 558 we simulated such a track in 90:10 Ar:CO₂ gas mixture, later we added a simu-
 559 lation in 70:30 Ar:CO₂, which we plan to use in our detector. The comparison of
 560 both simulations is in Fig. 2.1.

561 2.1.2 Grid-like testing sample

562 In order to test all steps of the reconstruction, a sample of tracks with a grid-like
 563 distribution of parameters was generated on MetaCentrum. Five sets of 9702
 564 tracks were generated with every combination of these parameters:

- 565 • electron and positron tracks,
- 566 • 11 different kinetic energies $E_{\text{kin}} \in [3, 13]$ MeV,
- 567 • 21 different azimuth angles $\varphi \in [-16.3^\circ, 16.3^\circ]$ and
- 568 • 21 different elevation angles $\theta \in [-17.1^\circ, 17.1^\circ]$.

569 A visualization of a set of e^+/e^- tracks with the same kinetic energy is shown
 570 in Fig. 2.2 (plotting actual HEED tracks using ROOT should be also possible
 571 (but hard to make look good?)). In the 70:30 Ar:CO₂ atmosphere, each track
 572 takes 5-30 CPU hours to simulate. Every tenth point on the drift line was stored,
 573 the whole sample has 3.1 terabytes (or 1.4 gigabytes without drift lines).

574 2.2 Runge-Kutta Simulation

575 The Runge-Kutta simulation in this work uses the Runge-Kutta 4th order (RK4)
 576 method to numerically integrate the equation of motion of a relativistic charged
 577 particle in an electromagnetic field. Given a system of first order differential
 578 equations

$$\frac{dy}{dt} = \mathbf{f}(t, \mathbf{y}(t)) \quad (2.1)$$

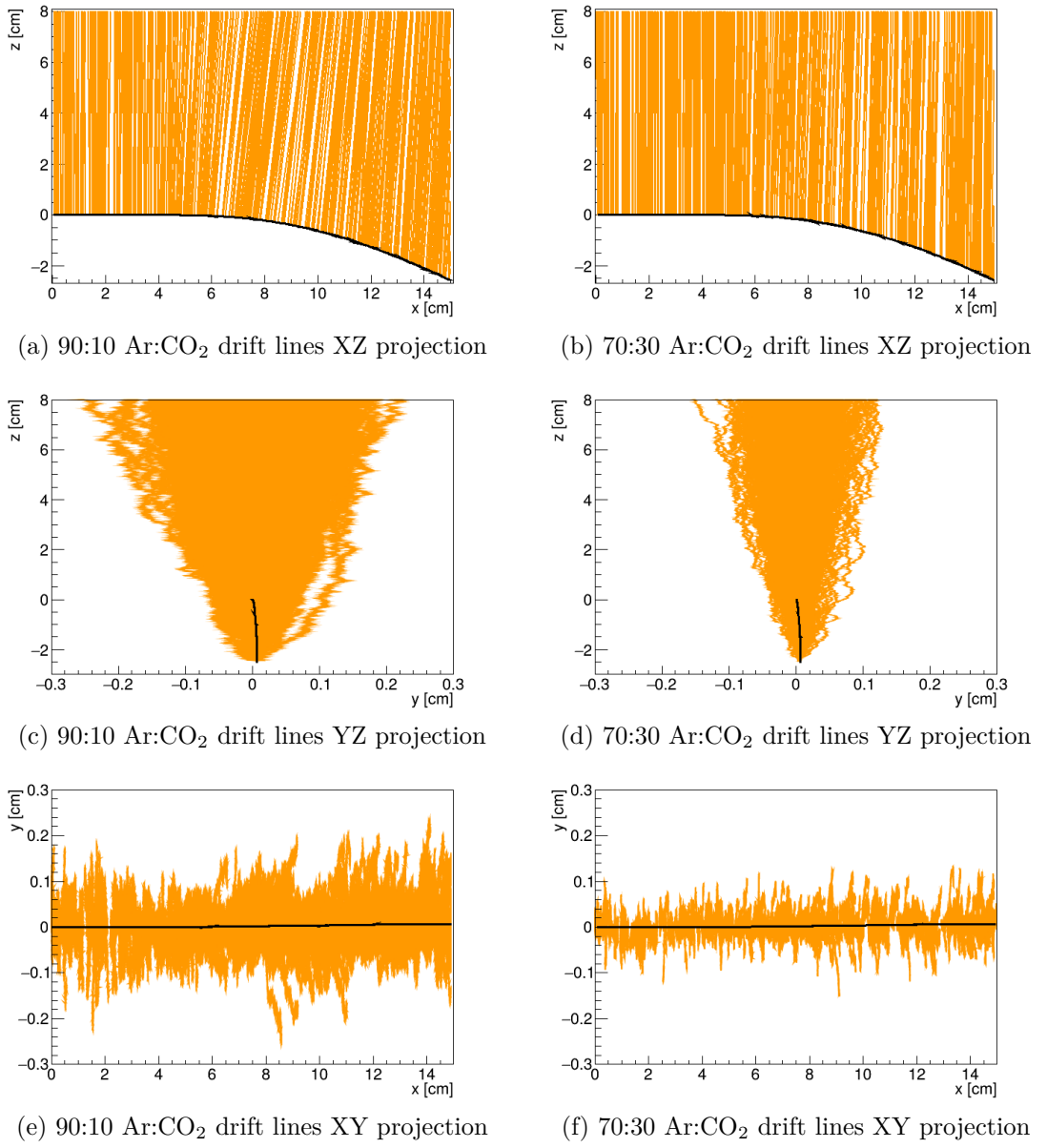


Figure 2.1: Comparison of drift lines for two different gas mixtures 90:10 and 70:30 Ar:CO₂. The electron track is marked in black, the drift lines of the ionization electrons are marked in orange. In this example, we assume a larger OFTPC volume with readout at $z = 8$ cm.

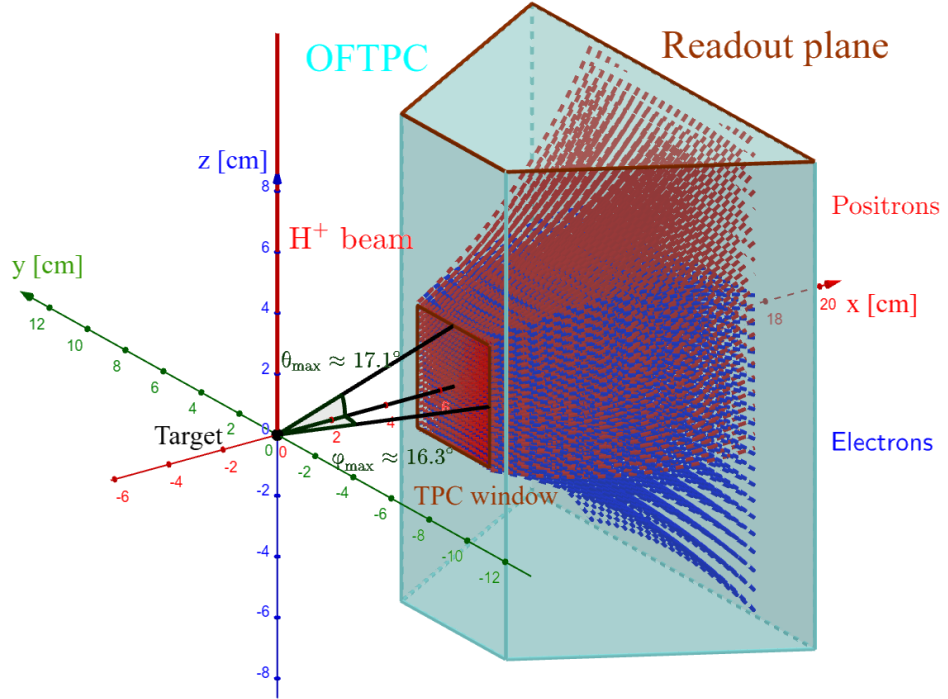


Figure 2.2: A visualization of a set of tracks from the grid-like testing sample with the same kinetic energy.

579 with an initial condition

$$\mathbf{y}(t_0) = \mathbf{y}_0, \quad (2.2)$$

580 we iteratively compute the estimate $\mathbf{y}_n = \mathbf{y}(t_n) = \mathbf{y}(t_0 + nh)$ as follows (citation?
581 common knowledge?):

$$\mathbf{k}_1 = \mathbf{f}(t_n, \mathbf{y}_n), \quad (2.3)$$

$$\mathbf{k}_2 = \mathbf{f}\left(t_n + \frac{h}{2}, \mathbf{y}_n + \frac{h\mathbf{k}_1}{2}\right), \quad (2.4)$$

$$\mathbf{k}_3 = \mathbf{f}\left(t_n + \frac{h}{2}, \mathbf{y}_n + \frac{h\mathbf{k}_2}{2}\right), \quad (2.5)$$

$$\mathbf{k}_4 = \mathbf{f}(t_n + h, \mathbf{y}_n + h\mathbf{k}_3), \quad (2.6)$$

582

$$\mathbf{y}_{n+1} = \mathbf{y}_n + \frac{1}{6}(\mathbf{k}_1 + 2\mathbf{k}_2 + 2\mathbf{k}_3 + \mathbf{k}_4). \quad (2.7)$$

583 Alternate forms (infinitely many) possible, accuracy vs computational cost. Runge-
584 Kutta-Fehlberg with adaptive step size also possible, can potentially save some
585 computation time especially in rapidly changing field (so maybe not in this case).

586 In our case, we want to integrate the equation of motion, given by the rela-
587 tivistic Lorentz force:

$$F_L^\mu = m \frac{du^\mu}{d\tau} = q F^{\mu\nu} u_\nu, \quad (2.8)$$

588 where the Einstein summation convention is used, m is the mass of the particle,
589 q is its charge, u^μ is its four-velocity, τ is the proper time (i.e., time in the particle's
590 frame of reference) and $F^{\mu\nu}$ is the electromagnetic tensor at given coordinates x^μ

591 (we consider it to be time-independent in our detector). Given the electric $\mathbf{E} =$
 592 $= (E_x, E_y, E_z)$ and the magnetic field $\mathbf{B} = (B_x, B_y, B_z)$ and using the metric
 593 signature $(+, -, -, -)$, the equation expands to

$$\frac{d}{d\tau} \begin{pmatrix} \gamma c \\ \gamma v_x \\ \gamma v_y \\ \gamma v_z \end{pmatrix} = \frac{q}{m} \begin{pmatrix} 0 & -\frac{E_x}{c} & -\frac{E_y}{c} & -\frac{E_z}{c} \\ \frac{E_x}{c} & 0 & -B_z & B_y \\ \frac{E_y}{c} & B_z & 0 & -B_x \\ \frac{E_z}{c} & -B_y & B_x & 0 \end{pmatrix} \begin{pmatrix} \gamma c \\ \gamma v_x \\ \gamma v_y \\ \gamma v_z \end{pmatrix}, \quad (2.9)$$

594 where c is the speed of light in vacuum, $\mathbf{v} = (v_x, v_y, v_z)$ is the particle's velocity
 595 and $\gamma = (1 - \frac{v^2}{c^2})^{-\frac{1}{2}}$ is the Lorentz factor (wrong magnetic field sign in the
 596 implementation???). Together with the equation

$$\frac{d}{d\tau} \begin{pmatrix} ct \\ x \\ y \\ z \end{pmatrix} = \begin{pmatrix} \gamma c \\ \gamma v_x \\ \gamma v_y \\ \gamma v_z \end{pmatrix} = u^\mu, \quad (2.10)$$

597 we get a system of eight first order differential equations for x^μ and u^μ , which
 598 we can integrate using the Runge-Kutta method described above. As a result of
 599 this integration, we get the position $\mathbf{x}(\tau_n)$, the velocity $\mathbf{v}(\tau_n)$ and the detector
 600 time $t(\tau_n)$ for every proper time $\tau_n = n\tau_{\text{step}}$. Integrating using the proper time
 601 means that the step size in t gets larger by the gamma factor $\frac{dt}{d\tau} = \gamma$ (maybe
 602 change it and integrate the detector time or adjust the step size accordingly). The
 603 only difference is in the step size (because t gets also calculated as it is among the
 604 8 variables). It might be even better to adjust the step size using approximate
 605 distance traveled. As initial conditions, we use the origin of the track
 606 (x_0, y_0, z_0) , the initial velocity direction vector $\mathbf{n} = (\cos \varphi \cos \theta, \sin \varphi \cos \theta, \sin \theta)$
 607 and the kinetic energy E_{kin} (initial parameters of the simulation (fit is in chapter
 608 4)), we then compute γ and $\|\mathbf{v}\|$:

$$\gamma = 1 + \frac{E_{\text{kin}}}{E_0}, \quad (2.11)$$

$$\|\mathbf{v}\| = c\sqrt{1 - \gamma^{-2}}. \quad (2.12)$$

609 2.2.1 Testing sample

610 Example of RK simulation – first testing track, randomized sample of 100000
 611 tracks (could also move them to circle 3D fit).

612 In order to test the simulation and reconstruction, a sample of 100 000 tracks
 613 with randomized parameters was generated:

- 614 • the Runge-Kutta step was set to 0.1 ns (proper time, which wouldn't be a
 615 problem but this way the "spatial" step depends on energy),
- 616 • the kinetic energy of the particle $E_{\text{kin}} \in [4, 12]$ MeV,
- 617 • the starting point of the track is a random point in the OFTPC window,

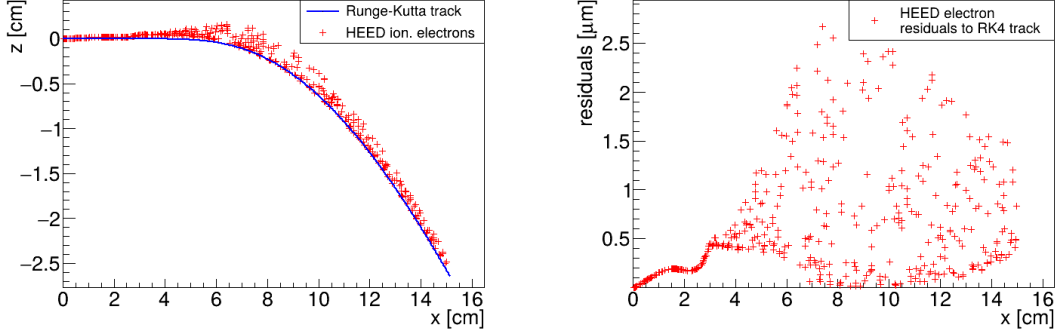


Figure 2.3: A comparison of the HEED track from the microscopic simulation in Section 2.1.1 with a Runge-Kutta track with the same initial parameters and $\tau_{\text{step}} = 0.1$ ps (reducing the step further doesn't make a visible difference). In the view of the tracks on the left, the distance of the HEED ionization electrons from the RK4 track is exaggerated 1000 \times . On the right, the dependence of the HEED electrons residuals (i.e., their shortest distance to the RK4 track) on their z -coordinate is shown. **The images look the same even for 100,000x smaller step, so the residuals are a result of something that HEED does (maybe a different interpolation technique for the magnetic field? the pattern looks similar for two different tracks so it can't be scattering).**

When exaggerating, the HEED ionization electrons are moved away along the shortest line connecting them to the RK4 track. The computation of this distance is described in Section 4.3.

- 618 • the initial direction is given by the line connecting a random point on
619 the target¹ (a disc with 1 mm radius in the YZ plane).
- 620 Since the Runge-Kutta simulation is quite fast², it can be run locally on any
621 computer. **Add a figure with simulated tracks (sample).** An example Runge-
622 Kutta track is compared with the corresponding microscopic track in Fig. 2.3.

¹To generate a random point on the target, we generate a random angle α and a random square of the distance from origin r^2 to get a uniform distribution.

²One track with $\tau_{\text{step}} = 0.1$ ps takes less than one millisecond to simulate.

623 3. Track Reconstruction

624 As the first step of the reconstruction algorithm, we reconstruct the track of
625 a primary particle – either an electron or a positron. Then, using this information,
626 we determine the energy of the particle (Section 4).

627 The **Reconstruction Assuming Steady Drift** uses the standard TPC ap-
628 proach. With parallel fields, the drift inside a uniform electric field remains
629 undistorted (as shown in Equation 1.1). Therefore, we only need to reconstruct
630 the z -coordinate from the drift time using the known drift velocity. We also
631 assume that the readout coordinates (x' , y' , t) are known exactly, neglecting
632 the pads and time binning.

633 Reconstruction using an **Ionization Electron Map** (from now on referred
634 to as *the map*) uses a simulation of the drift of secondary (ionization) electrons
635 within the detector volume. This simulation can then be used to interpolate
636 the initial position of the secondary electrons. In the first iteration of this method
637 the readout is assumed to be continuous.

638 We present two algorithms using the map for reconstruction. The first one uses
639 a gradient descent algorithm along with trilinear interpolation (see Section 1.4.3)
640 of the map. The second method uses interpolation on the irregular inverse grid
641 with a polynomial.

642 The **Discrete Reconstruction** uses the map; instead of reconstructing the ex-
643 act position of each electron, we reconstruct the center of each hit pad together
644 with the time corresponding to the midpoint of the time bin. The electron count
645 in each TPC bin (consisting of the pad and the time bin) serves as an idealized
646 collected charge, which is then used as a weight in the energy reconstruction fit.

647 3.1 Reconstruction Assuming Steady Drift

648 As the first step, we tried to reconstruct a simulated electron track with a special
649 set of initial parameters, described in detail in Section 2.1.1. The starting point
650 is given by the origin of our coordinate system and its initial direction is given by
651 the positive x -axis. This means the magnetic field of our detector is perpendicular
652 to the momentum of the particle at all times, and we can reduce the problem to
653 two-dimensional space.

654 For the reconstruction, we decided to use the common method used in a stan-
655 dard TPC (similar to?, cite some source(s)!). This will allow us to explore
656 the significance of the atypical behavior in our OFTPC. Additionally, we assume
657 the readout is continuous to further simplify the problem. In this approximation,
658 we reconstruct the initial position of each ionization electron.

659 The reconstruction is then defined by the following relations between the co-
660 ordinates of the detector space and the readout space (see Section 1.4.2):

$$x = x', \quad (3.1)$$

$$y = y', \quad (3.2)$$

$$z = 8 \text{ cm} - d_r = 8 \text{ cm} - v_d t, \quad (3.3)$$

661 where d_r is the distance to the readout, and v_d is the drift velocity of electrons
662 in the given gas mixture. At a phenomenological level, this velocity can be con-

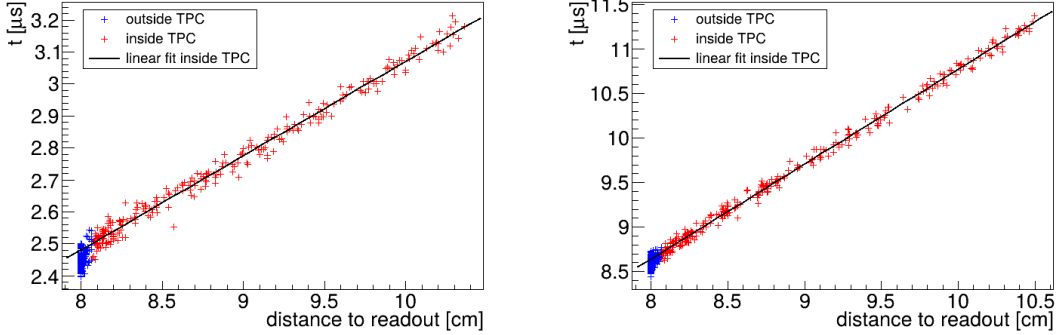


Figure 3.1: Linear fit of the drift time t dependence on the distance to the readout $d_r = 8 \text{ cm} - z$ for the ionization electrons in 90:10 (left) and 70:30 (right) Ar:CO₂ gas composition. Only electrons inside the TPC (red) are fitted. The parameters are $v_d = 3.39 \text{ cm}/\mu\text{s}$, $d_0 = -0.41 \text{ cm}$ for 90:10, and $v_d = 0.939 \text{ cm}/\mu\text{s}$, $d_0 = -0.11 \text{ cm}$ for 70:30 Ar:CO₂.

sidered as a function of the electric field \mathbf{E} and the magnetic field \mathbf{B} as shown in Equation 1.1. The Garfield++ toolkit uses this fact to accelerate their drift simulation with non-microscopic approaches (could mention in the simulation chapter). Since we assume a uniform electric field in the detector and in this approximation we want to neglect the effect of our unusual magnetic field, we consider the drift velocity constant. We can estimate the drift velocity by fitting the dependence $d_r(t)$ of ionization electrons from a simulated track with a linear function:

$$d_r(t) = v_d t + d_0. \quad (3.4)$$

The fit was applied on two tracks with different gas composition, the result is in Fig. 3.1. Compare with real drift velocities – a good indication of the tilt of drift lines. The obtained parameters are then used for the reconstruction shown in Fig. 3.2. From the residuals shown in Fig. 3.3, we can see that this reconstruction algorithm leads to significant deviations from the simulated track (up to 1.1 cm for 90:10, and up to 0.3 cm for 70:30 Ar:CO₂), especially in the faster gas mixture 90:10 (as expected – for a higher mean time between collisions in Equation 1.1, the effect of the magnetic field is bigger). These deviations are mainly caused by the shift in the x -coordinate due to the tilt of the drift lines in magnetic field. In order to account for this, we need to develop a better algorithm. There is also a small irregularity in the z -coordinate but it is comparable with the diffusion. We can/will also later show that this has a significant effect on the reconstructed energy.

3.2 Ionization Electron Map

Inside an OFTPC (more than one, also considering it a general concept rather than the specific OFTPC used at this experiment), the drift of the ionization electrons is significantly affected by its magnetic field as shown in Equation 1.1, see also Fig. 2.1. We need to take this into account for accurate reconstruction (should be easy to run the reconstruction without the map and show how much it improves the results). In the first approximation, we assume a continuous readout (i.e., we neglect the anode segmentation into pads). We can then

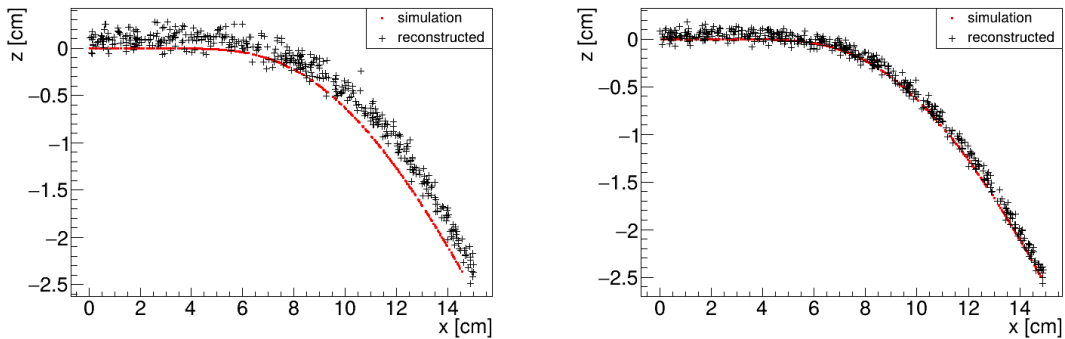


Figure 3.2: Reconstruction (black) of the starting position of ionization electrons (red) using parameters obtained from the fit (Fig. 3.1). Two gas compositions 90:10 (left) and 70:30 Ar:CO₂ (right) are compared.

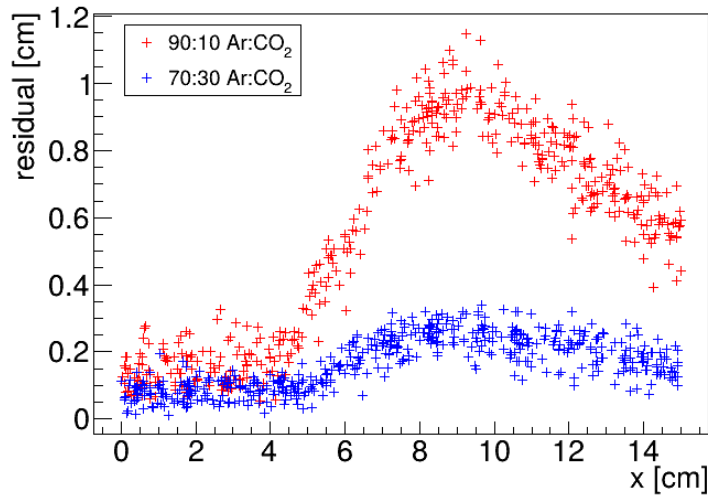


Figure 3.3: Comparison of residuals (i.e., the distance from the reconstructed point to the simulated ionization electron starting point) dependence on x for two gas mixtures 90:10 (red) and 70:30 Ar:CO₂ (blue).

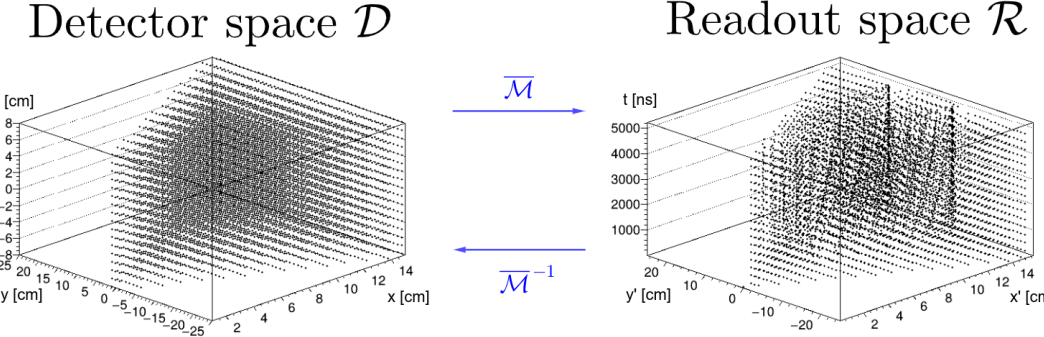


Figure 3.4: A 3D visualization of the mapping of means $\bar{\mathcal{M}}$ for the 90:10 Ar:CO₂ gas. A regular grid \mathbb{G} with $l = 1$ cm in the detector space is mapped to an irregular grid $\mathbb{G}^{-1} \equiv \bar{\mathcal{M}}(\mathbb{G})$ in the readout space.

691 reconstruct the original position of each ionization electron using its readout co-
692 ordinates. For this purpose, we use the ionization electron map.

693 The ionization electron map represents a mapping from the detector space
694 to the readout space (see Section 1.4.2). It tells us what readout coordinates
695 (x', y', t) we can expect on average for an ionization electron created at the detec-
696 tor coordinates (x, y, z). More precisely, it is a mapping to the distributions on
697 the readout space; we can simplify this as only the means $\bar{\mathcal{M}}$ and the covariance
698 matrices \mathcal{M}_Σ , assuming Gaussian distribution:

$$\bar{\mathcal{M}}: \mathcal{D} \longrightarrow \mathcal{R}, \quad (x, y, z) \longmapsto \bar{\mathbf{X}}^T \equiv (\bar{x}', \bar{y}', \bar{t}), \quad (3.5)$$

$$\mathcal{M}_\Sigma: \mathcal{D} \longrightarrow \mathbb{R}^{3 \times 3}, \quad (x, y, z) \longmapsto \Sigma \equiv \begin{pmatrix} \sigma_{x'}^2 & \text{cov}(x', y') & \text{cov}(x', t) \\ \text{cov}(y', x') & \sigma_{y'}^2 & \text{cov}(y', t) \\ \text{cov}(t, x') & \text{cov}(t, y') & \sigma_t^2 \end{pmatrix}, \quad (3.6)$$

$$\mathcal{M}: \mathcal{D} \longrightarrow D(\mathcal{R}), \quad (x, y, z) \longmapsto N(\mathbf{X}) \equiv \frac{\exp\left(-\frac{1}{2}(\mathbf{X} - \bar{\mathbf{X}})^T \Sigma (\mathbf{X} - \bar{\mathbf{X}})\right)}{\sqrt{(2\pi)^3 |\Sigma|}}. \quad (3.7)$$

699 To get an approximation of this mapping, we simulate the drift of ionization
700 electrons generated on a regular Cartesian grid $\mathbb{G} \subset \mathcal{D}$ with spacing l inside
701 the volume of our OFTPC¹ (see the visualization in Fig. 3.4). In Fig. 3.5, you
702 can see an example of drift lines from a test of the simulation. After testing runs,
703 two map simulations were made with different gas composition, their parameters
704 are shown in Table 3.1.

705 In order to get accurate results, we use the microscopic simulation of these
706 electrons described in Section 2.1 (Monte Carlo from *AvalancheMC* was also con-
707 sidered but it doesn't (didn't? CERES used it from MAGBOLTZ???) include
708 magnetic field, we can probably improve this anyway using the fast track sim-
709 ulation with map proposed in the future section). It is also useful to simulate
710 multiple (N) electrons originating from the same position so that we can account
711 for the random fluctuations due to collisions. Using the readout coordinates of
712 the electrons, we then estimate the means and the covariance matrix:

$$\bar{\mathbf{X}} = \frac{1}{N} \sum_{i=1}^N \mathbf{X}_i, \quad \Sigma = \frac{1}{N-1} \sum_{i=1}^N (\mathbf{X}_i - \bar{\mathbf{X}})(\mathbf{X}_i - \bar{\mathbf{X}})^T, \quad (3.8)$$

¹The detector walls are not considered and we simulate the drift even outside of the OFTPC which allows us to interpolate even close to the walls

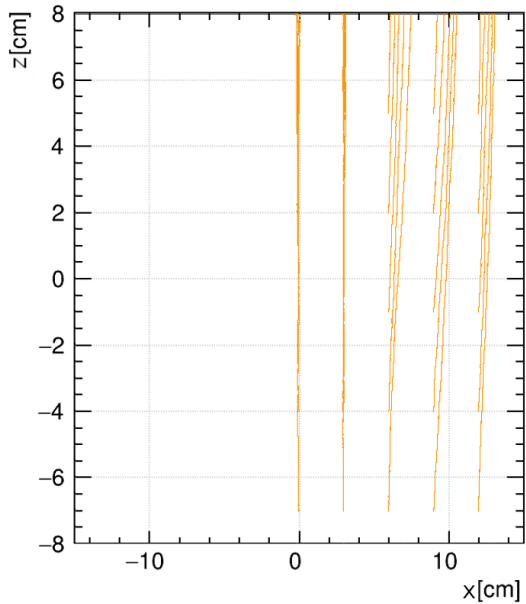


Figure 3.5: A test of the 90:10 Ar:CO₂ map simulation with spacing $l = 1.5$ cm. The resulting drift lines of evenly spaced electrons are displayed in orange.

Table 3.1: Comparison of parameters of two map simulations.

Parameter	90:10 Ar:CO ₂ map	70:30 Ar:CO ₂ map
N	100	100
l	1.0 cm	0.5 cm
z bounds	$[-8, 8]$ cm	$[-8, 8]$ cm
x bounds	$[0, 15]$ cm	$[-1.5, 15.0]$ cm
y bounds	$ y \leq x \cdot \tan \frac{\pi}{3}$	$ y \leq (x + 1.5 \text{ cm}) \cdot \tan \frac{\pi}{6}$

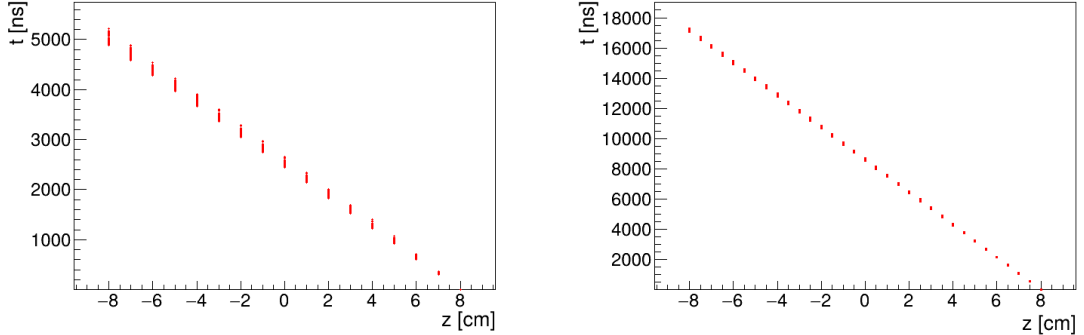


Figure 3.6: Dependence of the drift times of the simulated map $\bar{\mathcal{M}}$ on the z -coordinate. Two gas mixtures 90:10 (left) and 70:30 Ar:CO₂ (right) are compared. The spread is caused by varying Lorentz angles.

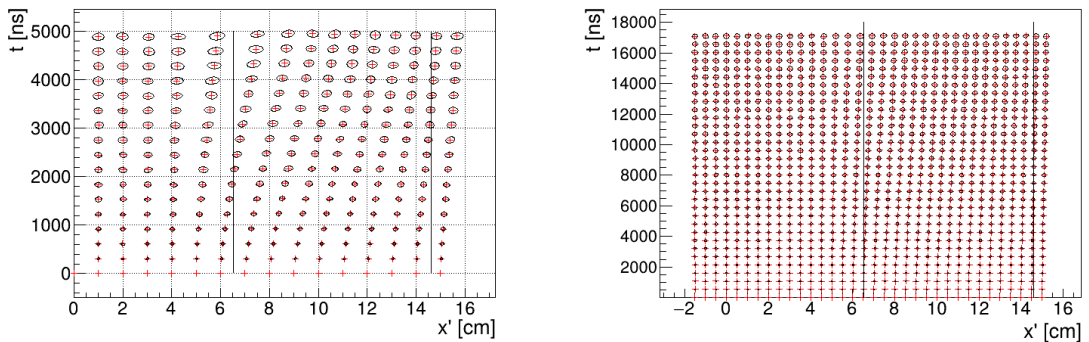


Figure 3.7: The $x't$ projection of the $\mathcal{M}(\mathbb{G}_{y=0})$ mapping of a part of the regular grid \mathbb{G} . The means $\bar{\mathcal{M}}(\mathbb{G}_{y=0})$ are marked with red crosses, and the diffusion error is denoted by black 95% confidence error ellipses computed from the diagonalized covariance matrices $\mathcal{M}_\Sigma(\mathbb{G}_{y=0})$. Two gas mixtures 90:10 (left) and 70:30 Ar:CO₂ (right) are compared. The first mixture shows differences of t for electrons with same initial z but different initial x . For the second mixture, these differences are negligible in comparison with the diffusion.

713 where \mathbf{X}_i represents the readout coordinates $(x'_i, y'_i, t_i)^T$ of the i -th electron. The
 714 matrix (resp. its submatrix) can then be used to plot error ellipsoid (resp. el-
 715 llsoid). The axes correspond to the eigenvectors, errors along these axes for a given
 716 confidence level p can be computed using the chi-squared distribution

$$\sigma_i = \sqrt{\lambda_i \chi_k^2(p)}, \quad (3.9)$$

717 where λ_i is the corresponding eigenvalue and k is the number of degrees of free-
 718 dom.

719 As shown in Figs. 3.6 and 3.7, the drift times in the map are no longer propor-
 720 tional to the z -coordinate due to the varying Lorentz angles in the inhomogeneous
 721 magnetic field (see Equation 1.2). As expected, the effect is considerably larger in
 722 gases with higher drift velocities. Similarly, the drift distortion (i.e., its deviation
 723 from the vertical lines) is huge for the "faster" gas, but still significant for the
 724 "slower" one, as demonstrated in Figs. 3.8 to 3.10.

725 When evaluating the map inside the grid, we use trilinear interpolation (see
 726 Section 1.4.3). From now on, we will use the same symbol \mathcal{M} for this interpolated

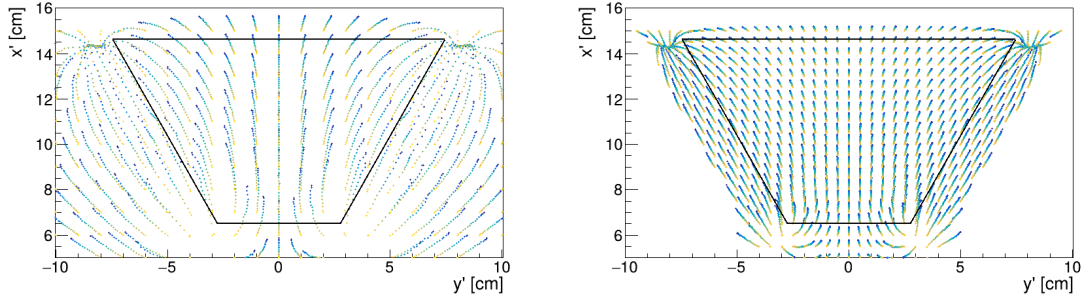
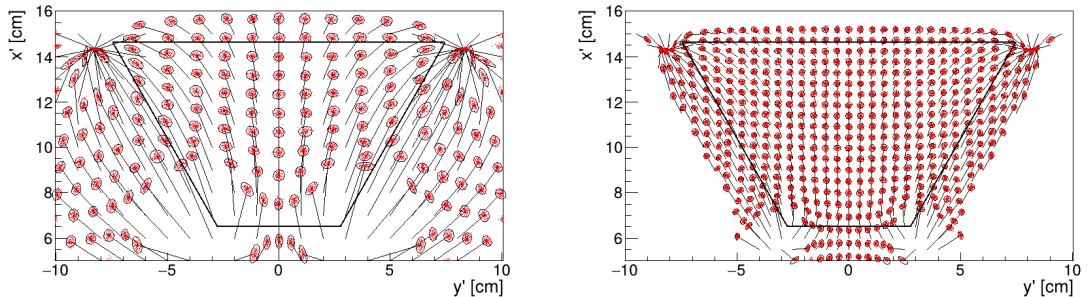
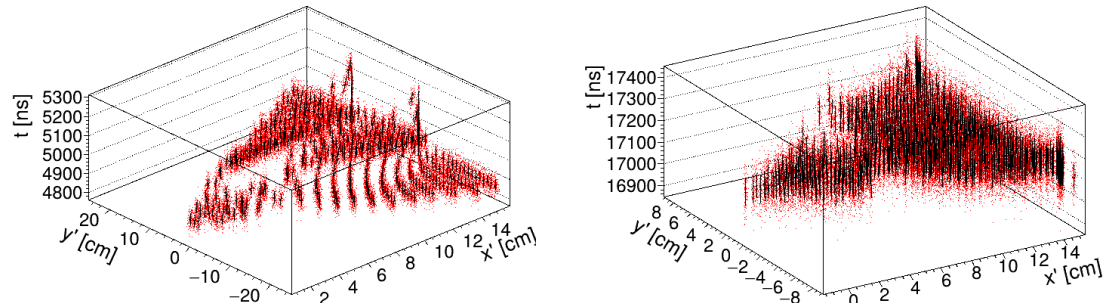


Figure 3.8: The regular grid \mathbb{G} projected by the mapping $\bar{\mathcal{M}}$ from the detector space onto the $x'y'$ plane (t is not plotted). Layers with lower z -coordinate (i.e., further away from the readout) are displayed with darker colors. The OFTPC volume is marked with black lines. Two gas mixtures 90:10 (left) and 70:30 Ar:CO₂ (right) are compared.



(a) The $x'y'$ projection of $\mathcal{M}(\mathbb{G}_8)$ (similar as in Fig. 3.8), the diffusion is denoted with the 95% error ellipses from the diagonalized sample covariance matrices $\mathcal{M}_{\Sigma}(\mathbb{G}_8) \leftrightarrow$ Equation 3.8, and computed using Equation 3.9. The mean values $\bar{\mathcal{M}}(\mathbb{G}_8)$ are connected by black arrows with the corresponding starting position (x, y) of the simulated electrons. The OFTPC volume is marked with black lines.



(b) The full mapping $\mathcal{M}(\mathbb{G}_8)$, the diffusion is marked using standard error bars (black) from the diagonalized sample covariance matrices (Equations 3.8 and 3.9).

Figure 3.9: The $\mathcal{M}(\mathbb{G}_8)$ mapping of the bottom ($z = -8$ cm) layer \mathbb{G}_8 of the regular grid $\mathbb{G} \subset \mathcal{D}$. It includes both the mapping of means $\bar{\mathcal{M}}$ and of covariances \mathcal{M}_{Σ} . Individual electrons from the map simulation are marked with red dots. Two gas mixtures 90:10 (left) and 70:30 Ar:CO₂ (right) are compared.

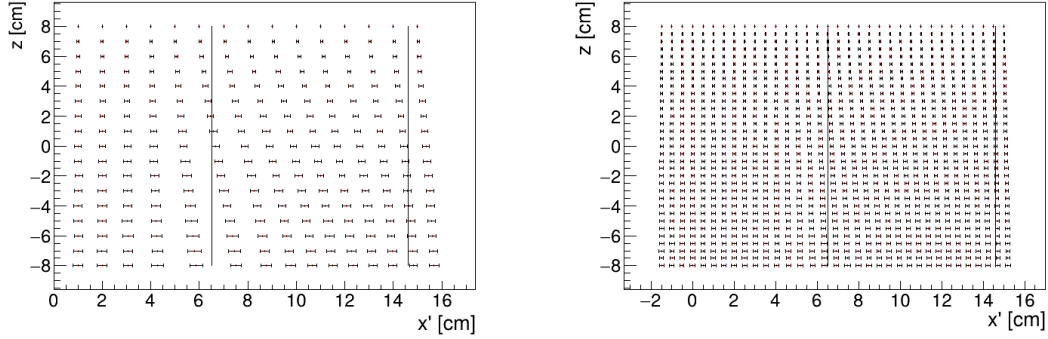


Figure 3.10: The readout coordinate x' for points on the grid $\mathbb{G}_{y=0}$ plotted against their initial coordinate z . The means are marked with red crosses, the diffusion in x' is denoted by standard error bars. Two gas mixtures 90:10 (left) and 70:30 Ar:CO₂ (right) are compared.

727 simulation.

728 Finally, we need to invert the map to get the original detector coordinates
 729 (x, y, z) from the given readout coordinates (x', y', t) . In our case, it is reasonable
 730 to assume that the mapping \mathcal{M} (we lose the information about the distribution
 731 (a wild idea how to recover this is in the Future section but it will only make sense
 732 if the GEM is already accounted for and is very preliminary as there are many
 733 factors to consider)) is one-to-one (as seen in the simulations). We implemented
 734 two methods for this purpose: the gradient descent search (Section 3.2.1) and
 735 interpolation on the inverse grid (Section 3.2.2).

736 The simulation (?) of the map is a computationally heavy task. For this rea-
 737 son, we use the MetaCentrum grid [3] to parallelize needed calculations. At first,
 738 this was done by evenly distributing the simulated electrons across the individual
 739 jobs in a simulation with only one electron per vertex in the regular grid \mathbb{G} with
 740 a spacing of one centimeter. Later, a more efficient approach was implemented,
 741 accounting for the varying lengths of the drift of individual electrons. If we index
 742 the vertices of \mathbb{G} in the order of increasing coordinates y, x, z (picture will make
 743 things clearer), we can express the number n_l of full XY layers (i.e., electrons
 744 with the same z coordinate, the mapping of one such layer is shown in Fig. 3.9b)
 745 with index less than or equal to i

$$n_l(i) = \left\lfloor \frac{i}{n_{xy}} \right\rfloor, \quad (3.10)$$

746 where n_{xy} is the number of electrons in each XY layer calculated simply by count-
 747 ing the electrons that satisfy boundary conditions for x and y . These conditions
 748 should be mentioned above; sector condition + maximal x value. The number of
 749 electrons remaining in the top layer is then

$$n_r(i) = i \bmod n_{xy}. \quad (3.11)$$

750 Finally, we can calculate the sum of the drift gaps of electrons up to index i

$$d_{\text{sum}} = (z_{\max} - z_{\min})n_{xy}n_l - \frac{n_l(n_l - 1)}{2}n_{xy}l + n_r(z_{\max} - z_{\min} - n_l l). \quad (3.12)$$

751 We then use a binary search algorithm to find the maximum index i such that
 752 the value of this sum is less than the fraction $\frac{\text{job id}}{\max \text{ job id}}$ of the total sum. This way
 753 we obtain the minimal and the maximal index of electrons simulated in the given
 754 job. **Picture of the simulating grid (1 layer).** zmin zmax also

755 The obtained map is then stored in a custom class template *Field*, could
 756 expand on that. Maybe earlier, since the same template is used for the magnetic
 757 field.

758 Simulation inside of one sector (at first double angle). Extra space on the sen-
 759 sor. Using qsub (not sure if important). Add plots of distortion of the coordinates.
 760

761 Images to add (comparison of both simulations):

- 762 Already have a simple 2D map visualization from the RD51 presentation,
 763 can use it or make something better
- 764 • z vs. t plot
- 765 • XY plane distortion for different z values; with arrows and error bars, for
 766 all z -layers with different colors
- 767 • XZ plane ($y = 0$) distortion in x (maybe not necessary?)
- 768 • XT plot ($y = 0$) showing (small) distortion in drift times
 769

770 More images:

- 771 • Residuals of the continuous readout reconstruction.

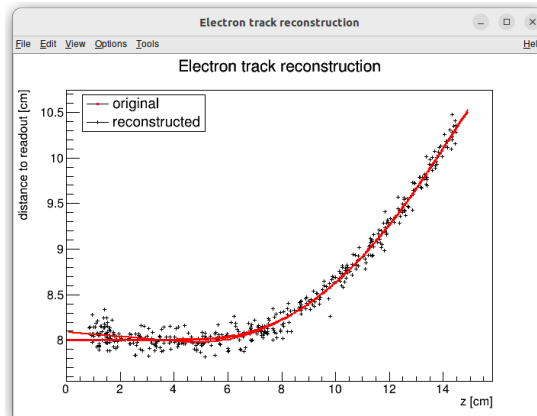


Figure 3.11: Example reconstruction with the map. Swap for better image, correct coordinates.

772 3.2.1 Gradient Descent Algorithm

773 The first implemented method of reconstruction uses a gradient descent algorithm
 774 to calculate an inversion of the map $\bar{\mathcal{M}}$ in a given point. Gradient descent is
 775 an iterative minimization algorithm for multivariate functions. Let $R \in \mathcal{R}$ be
 776 a point in the readout space; we want to find a point $D = (x, y, z) \in \mathcal{D}$ in
 777 the detector space such that

$$\bar{\mathcal{M}}(D) = R = (x'_R, y'_R, t_R). \quad (3.13)$$

778 We define a function f_R in the readout space as a distance in this space:

$$f_R(x', y', t) = \sqrt{(x' - x'_R)^2 + (y' - y'_R)^2 + v_d^2(t - t_R)^2}, \quad (3.14)$$

779 where v_d is an approximation of the drift velocity in the TPC, obtained from
780 the reconstruction in Section 3.1 (there will be an image with the linear fit here).

781 We make an initial guess (actually in the original code we just take $z = 0$):

$$D_0 = (x'_R, y'_R, v_d t). \quad (3.15)$$

782 Assuming we have the n -th estimate D_n , we calculate the i -th component of
783 the gradient of $f_R \circ \bar{\mathcal{M}}$ numerically using central differences: (signs look correct)

$$[\nabla(f_R \circ \bar{\mathcal{M}})]^i(D_n) \approx \frac{f_R(\bar{\mathcal{M}}(D_n + s \cdot e^i)) - f_R(\bar{\mathcal{M}}(D_n - s \cdot e^i))}{2s}, \quad (3.16)$$

784 where $e^i \in \mathcal{D}$ is the i -th coordinate vector and s is the step size. The step size
785 should be sufficiently small; initially, we set it as a fraction $s = \frac{l}{10}$ of the map's
786 grid spacing l . During the minimization, we check that $f_R(\bar{\mathcal{M}}(D_n)) < 10s$ at all
787 times (s can (?) change – check). When using trilinear interpolation, it would be
788 more efficient to calculate the gradient explicitly (\pm same result). This could be
789 implemented inside the *Field* template class. The next iteration can be calculated
790 as follows:

$$D_{n+1} = D_n - \gamma \nabla(f_R \circ \bar{\mathcal{M}})(D_n), \quad (3.17)$$

791 where $\gamma \in \mathbb{R}^+$ is the damping coefficient. It should be set to a small enough
792 value to ensure convergence, but large enough for sufficient converging speed.
793 The minimization stops either when the error $f_R(\bar{\mathcal{M}}(D_n))$ drops below a specified
794 value or when the number of iterations exceeds a certain limit (in this case,
795 a message is printed into the console). The parameters of this method can be
796 further optimized (e.g., a better choice of γ , gradient computation); instead, we
797 later decided to use the interpolation on the inverse grid described in the next
798 section.

799 Measure reconstruction duration and compare it with the inverse grid inter-
800 polation? Also compare the result? Typical evolution of D_n during search. Not
801 sure if this has to be cited.

802 3.2.2 Interpolation on the Inverse Grid

803 Interpolation should be generally faster than the gradient descent since we don't
804 need to iterate. We also don't need to optimize it to improve performance, if
805 it's too slow we can even calculate the coefficients for the entire map before
806 reconstruction (again, do some profiling).

807 The best current algorithm uses the interpolation on the inverse grid. Rather
808 than inverting the trilinearly interpolated map using a numerical minimization
809 method as in the previous section, we take advantage of the fact that the map
810 $\bar{\mathcal{M}}$ is one-to-one (isomorphism is supposed to preserve structure, not sure how
811 to interpret that here, not the best description, we already (kind of) assume it
812 is a bijection by saying we will invert it). Since we have simulated values of this
813 map on a regular grid in the detector space \mathcal{D} , we also know the inverse map $\bar{\mathcal{M}}^{-1}$

814 on the irregular inverse grid in the readout space \mathcal{R} . To get an approximation
 815 of the inverse map in the entire readout space, we can use interpolation (**general**
 816 **concept, the specific choice is described below**).

817 Since the inverse grid is irregular, trilinear interpolation cannot be applied.
 818 Given that the simulated map is dense enough to provide a good approximation
 819 considering the size of our pads, we can adopt a similar approach.² As shown in
 820 Equation 1.21 in Section 1.4.3, trilinear interpolation (**shouldn't need an article**
 821 **when talking about a general concept**) can be expressed as a polynomial:

$$\hat{f}(x, y, z) = axyz + bxy + cxz + dyz + ex + fy + gz + h, \quad (3.18)$$

822 where a, b, c, d, e, f, g, h are coefficients uniquely determined by the values of
 823 the function at the vertices of the interpolation cell (**can be calculated in the**
 824 **way shown in the mentioned equation, not sure what more to add**). We can gen-
 825 eralize this for a function defined on an irregular grid. Given the function values
 826 at any eight points, we can write a system of eight linear equations

$$\begin{pmatrix} x_1y_1z_1 & x_1y_1 & x_1z_1 & y_1z_1 & x_1 & y_1 & z_1 & 1 \\ \vdots & \vdots \\ x_8y_8z_8 & x_8y_8 & x_8z_8 & y_8z_8 & x_8 & y_8 & z_8 & 1 \end{pmatrix} \begin{pmatrix} a \\ \vdots \\ h \end{pmatrix} = \begin{pmatrix} f(x_1, y_1, z_1) \\ \vdots \\ f(x_8, y_8, z_8) \end{pmatrix}, \quad (3.19)$$

827 which has a unique solution for the coefficients for most values of (x_n, y_n, z_n) and
 828 $f(x_n, y_n, z_n)$, where $n \in \{1, \dots, 8\}$.

829 This approach introduces a small complication: finding the correct pseudo-
 830 cell (i.e., the image of eight vertices forming a cubic cell in the regular grid) in
 831 the inverse grid. The eight irregularly spaced vertices of this pseudocell do not
 832 define a unique volume, so there are multiple possible ways to partition \mathcal{R} into
 833 pseudocells, with no obvious choice among them.

834 We are currently ignoring this problem and performing binary search along
 835 x, y, z (in this order). It shouldn't matter too much because the 70/30 map
 836 doesn't cause such a big distortion and was even accidentally extrapolated for all
 837 z different from the central plane.

²A more complicated and computationally heavy alternative would be natural neighbor interpolation or Kriging.

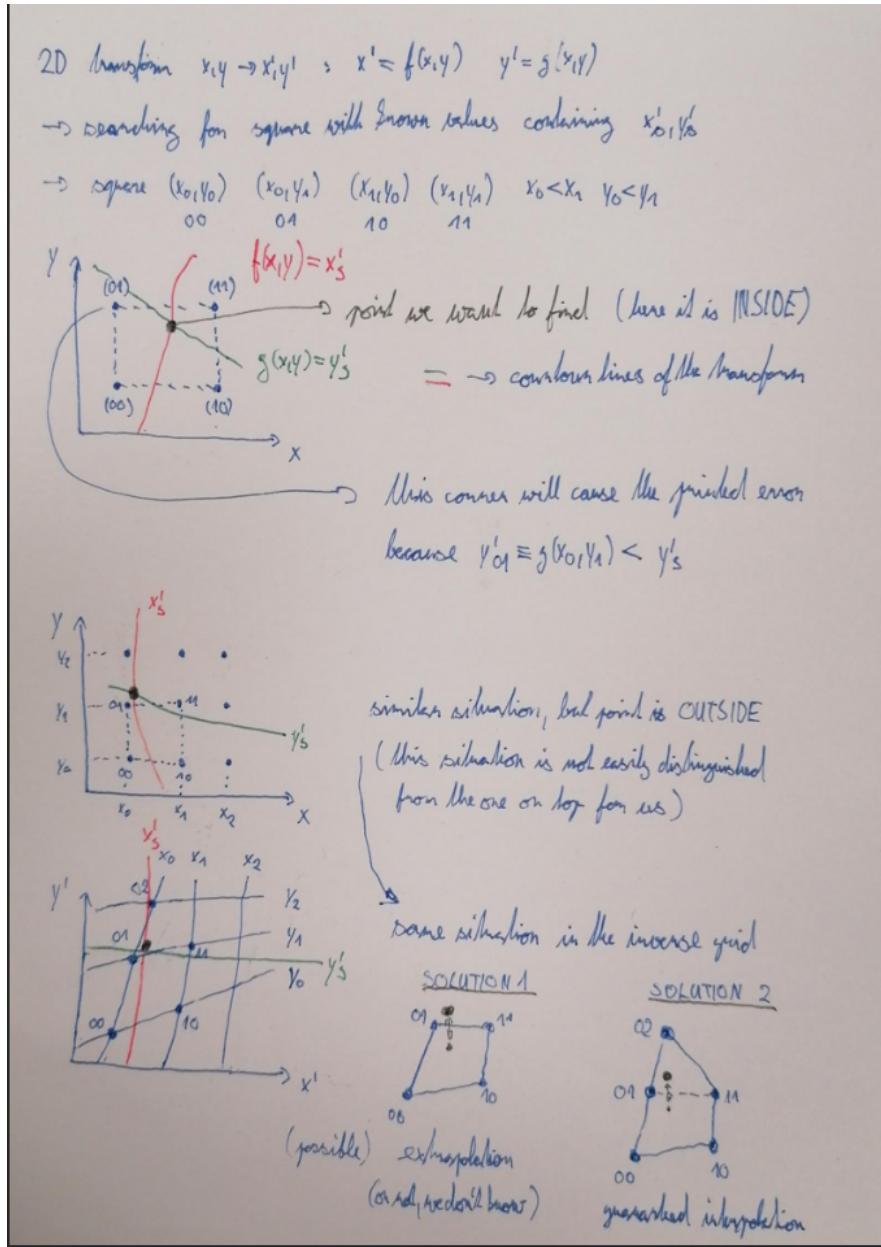


Figure 3.12: Selection of the points for interpolation. Create better images; use the explanation interpolation vs. extrapolation strange property. Solution 2 probably does not make much sense.

3.3 Discrete Reconstruction

Reconstruction with pads and time bins. Maybe testing different pads.

It is also possible to make this a subsection of the map, making the previous subsections parts of a new subsection 'Map Inversion'.

In order to get a more realistic representation of a track measured in the OFTPC, we need to take the discretization of the position and time data into account. The readout of the OFTPC will consist of 128 pads, their layout is shown in Fig. 1.7. Time is read out in discrete bins of size $t_{\text{bin}} = 100$ ns.

As the first approximation, we can neglect the multiplication in the triple-GEM.

and assume an ideal charge readout. The time measurement starts at the beginning of the electron/positron simulation (depending on the specific simulation it can correspond to the production in the target or when entering the OFTPC, here the specific time doesn't matter too much since the primary particle travels basically at light speed (30 ps/cm) which is circa immediate given the time binning). Randomize this time a bit and see what it does to the reconstruction. The readout coordinates $(x', y', t) \in \mathcal{R}$ of each ionization electron can be mapped to the pad coordinates $(n_{\text{pad}}, n_t) \in \mathcal{P}$:

$$n_{\text{pad}} = n: (x', y') \in \left[x_{1,n} - \frac{g}{2}, x_{2,n} + \frac{g}{2} \right] \times \left[y_{1,n} - \frac{g}{2}, y_{2,n} + \frac{g}{2} \right], \quad (3.20)$$

$$n_t = \left\lceil \frac{t}{t_{\text{bin}}} \right\rceil, \quad (3.21)$$

where $x, y_{1,n}$ and $x, y_{2,n}$ are the opposing pad corner coordinates, and g is the gap between the pads (described in detail in Section 1.4.2). This way, the closest pad is assigned to each readout position within the OFTPC volume³. Makes sense since the pads attract the electrons, the inhomogeneity of electric field is neglected. The number of electrons collected by each pad (i.e., collected charge) in each time bin is then counted and serves as a weight for the energy reconstruction. The reconstructed track consists of points for each $(n, n_t) \in \mathcal{P}$, we get these by reconstructing the position of a hypothetical electron with the readout coordinates of the pad/time bin center.⁴

$$\mathcal{D} \ni (x, y, z) = \overline{\mathcal{M}} \left(x_{c,n}, y_{c,n}, \left(n_t - \frac{1}{2} \right) t_{\text{bin}} \right). \quad (3.22)$$

³Some positions near the wall are not handled and some pads extend beyond the OFTPC volume. This is where an electric field simulation would come in handy.

⁴Mapping the center of the pad (along with the midpoint of the time bin) isn't necessarily the best approach since it might not correspond to the average parameters of an electron with these readout parameters.

864 4. Energy Reconstruction

865 The second stage is the reconstruction of the particle's energy using a fit of its
866 reconstructed track (see Section 3). We have tested three ways of reconstructing
867 the energy. Fitting is done using the MINUIT algorithm implemented in
868 ROOT [2]. Cite some CERN article directly on MINUIT, can add a section. Or
869 is it done using MIGRAD? The circle and RK4 probably was.

870 The **Cubic Spline Fit** was a tested and later rejected method of energy reconstruction.
871 It uses smoothly connected piecewise cubic polynomials between uniformly spaced nodes.
872 The reconstructed energy is calculated using the fit parameters by computing the radius of curvature in different points of the fitted
873 curve using the known magnitude of the magnetic field perpendicular to the trajectory.
874 We rejected this method because the tuning of the fit turned out to be unpractical compared to the other used methods. Reconstructs energy at every
875 position (even though the actual energy doesn't change much) and it might be slower but no profiling has been done yet. Of course, it wasn't tested on the
876 newer track reconstruction methods at all.

877 The **Circle and Lines Fit** was chosen as an alternative since this corresponds to the shape of a trajectory of a charged particle crossing a finite volume
878 with a homogeneous magnetic field. The energy of the particle can be estimated
879 using the fitted radius and the magnitude of the perpendicular magnetic field in the middle of the TPC.

880 The **Runge-Kutta Fit** uses the 4th order Runge-Kutta numerical integration described in Section 2.2. Initial parameters of the track (including the particle's energy) are optimized so that the integrated trajectory fits to the reconstructed one. This fit can also be performed as a single parameter (i.e., energy) fit if we get the initial position and orientation of the particle on the entrance to the TPC from previous detectors (TPX3 and MWPC, see Section 0.2).

891 4.1 Cubic Spline Fit

892 The first method for the estimation of the kinetic energy of the particle uses
893 a cubic spline fit. We use an electron track simulated using the microscopic

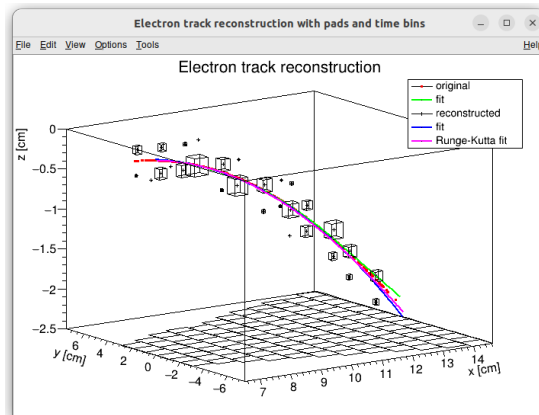


Figure 4.1: Example of a fitted reconstructed track. Swap for better image.

simulation, described in detail in Section 2.1.1. The track was reconstructed using the map described in Section 3.2.

In order to calculate the spline, we use the class *TSplines3* from ROOT. This allows us to evaluate the spline using the coordinates (x_n, z_n) of each node and the derivatives d_1, d_2 in the first and the last node. We can fit these parameters of a fixed amount of nodes to the simulated trajectory. We use the IMPROVE algorithm provided by the *TMinuit* class in ROOT (there are some guidelines for fonts in MFF UK template (Czech version) that I will eventually apply (see notes in the conclusion)). This algorithm attempts to find a better local minimum after converging (could reformulate a bit, taken word for word from some manual).

After the fit converges, we calculate an energy estimate using the radius of curvature, which we can extract from the fitted spline equation at every point of the trajectory. The part of the spline corresponding to a given node is defined as

$$z(x) = z_n + b\Delta x + c(\Delta x)^2 + d(\Delta x)^3, \quad (4.1)$$

where $\Delta x = x - x_n$ and b, c, d are coefficients. Using this equation, we derive the radius of curvature¹ as:

$$r(x) = \frac{(1 + z'^2(x))^{\frac{3}{2}}}{z''(x)} = \frac{(1 + (b + 2c\Delta x + 3d(\Delta x)^2)^2)^{\frac{3}{2}}}{2c + 6d\Delta x}. \quad (4.2)$$

Based on the geometry of our detector, we assume that the magnetic field satisfies $\mathbf{B}(x, 0, z) = (0, B(x, z), 0)$ for a track in the XZ plane. Since the electron is relativistic, the effect of the electric field on its trajectory is negligible. The Lorentz force F_L is then always perpendicular to the momentum of the electron and acts as a centripetal force F_c (not quite sure how to handle this then?):

$$\begin{aligned} \mathbf{F}_L &= \mathbf{F}_c, \\ \|e\mathbf{v} \times \mathbf{B}\| &= \frac{\gamma m_e v^2}{r}, \\ ec\beta B &= \frac{E_{0e}\beta^2}{r\sqrt{1 - \beta^2}}, \\ \sqrt{1 - \beta^2} &= \frac{E_{0e}\beta}{ecBr}, \end{aligned} \quad (4.3)$$

$$\beta^2(x) = \left[1 + \left(\frac{E_{0e}}{ecB(x, z(x))r(x)} \right)^2 \right]^{-1}, \quad (4.4)$$

where e is the elementary charge, c is the speed of light in vacuum, m_e is the rest mass of electron, $E_{0e} = m_e c^2$ is its rest energy, γ is the Lorentz factor, \mathbf{v} is the velocity of the electron, and $\beta = \frac{v}{c}$. The kinetic energy for a given point on the trajectory is then given as

$$E_{\text{kin}}(x) = \left(\frac{1}{\sqrt{1 - \beta^2(x)}} - 1 \right) E_{0e}. \quad (4.5)$$

¹For the general formula see https://en.wikipedia.org/wiki/Curvature#Graph_of_a_function.

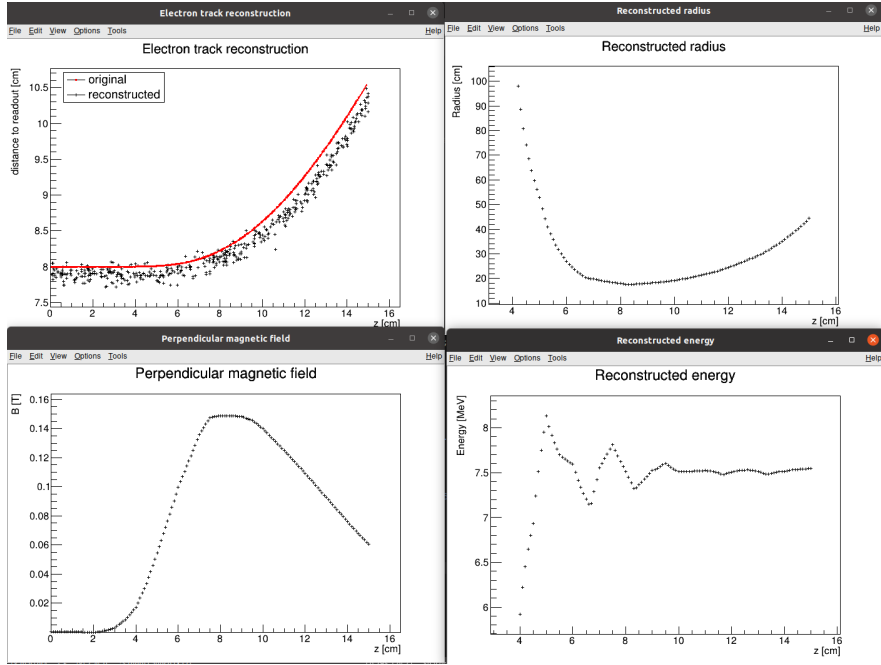


Figure 4.2: First attempt at a track reconstruction using only the drift velocity. Spline energy reconstruction attempt. Swap for better image(s) – subfigure environment, correct coordinates.

918 We can then average these estimates at multiple points (possibly using some
 919 weights to account for the change in accuracy, this wasn't optimized and we just
 920 ended with the graph) to get a single value. This method was later rejected in
 921 favor of the circle and lines fit (the name was already established at the beginning
 922 of the chapter) described in the next section. Add some figures.

923 4.2 Circle and Lines Fit

924 Another way to estimate the particle's kinetic energy is to fit its (??) trajectory
 925 with a circular arc with lines attached smoothly. This shape of trajectory cor-
 926 responds to a movement of a charged particle through a homogeneous magnetic
 927 field perpendicular to the particle's momentum and limited to a certain volume.
 928 In general, the shape of such a trajectory with a non-perpendicularly oriented
 929 momentum is a spiral. In our case, the magnetic field is approximately toroidal
 930 and the particle motion is nearly perpendicular to it (verify, could add some
 931 magnetic field plots in different vertical planes; shouldn't have a big effect on the
 932 reconstructed radius anyway). At first, we tested a 2D version of this fit, then
 933 we adapted it to 3D.

934 The field in our detector is not homogeneous, it is therefore not entirely clear
 935 what value of magnetic field should be used along with the fitted radius (using
 936 equations 4.4 and 4.5) to get the best estimate for the kinetic energy. Since we
 937 only use this method as the first iteration of the particle's energy that we later
 938 refine, an optimal solution of this problem is not required. Instead, we tested two
 939 options: taking the value of the field in the middle of the fitted circular arc (or
 940 is it in the middle x of the OFTPC?) and taking the average field along it. We

haven't really tried to plot this for multiple tracks, but these estimates are saved somewhere and could be plotted.

4.2.1 Two-dimensional fit

In the 2D case, the fitted function used for the electron track² described in Section 2.1.1 (one specific track at the time, technically this function doesn't work for a curvature that gets outside of the semicircle) is defined as follows:

$$z(x) = \begin{cases} a_1x + b_1 & x < x_1 \\ z_0 + \sqrt{r^2 - (x - x_0)^2} & x_1 \leq x \leq x_2 \\ a_2x + b_2 & x > x_2 \end{cases}, \quad (4.6)$$

where $a_{1,2}$ and $b_{1,2}$ are the parameters of the lines, (x_0, z_0) is the center of the circle, r is its radius, and $(x_{1,2}, z_{1,2})$ are the coordinates of the function's nodes. That means we have 9 parameters ($z_{1,2}$ are not used in the function) along with 2 continuity conditions and 2 smoothness conditions (9 parameters of the described function, 5 of them independent after taking the conditions into account). For the fit, we use the coordinates of the nodes and the radius of the circle, which gives us 5 independent parameters (only the radius has to be larger than half of the distance between nodes). The continuity conditions (combined with the relations for $z_{1,2}$) are

$$z_{1,2} = a_{1,2}x_{1,2} + b_{1,2} = z_0 - \sqrt{r^2 - (x_{1,2} - x_0)^2}, \quad (4.7)$$

the smoothness conditions are

$$a_{1,2} = \frac{x_0 - x_{1,2}}{\sqrt{r^2 - (x_{1,2} - x_0)^2}}. \quad (4.8)$$

Together with the Equation 4.7 we get the values of $b_{1,2}$

$$b_{1,2} = z_{1,2} - a_{1,2}x_{1,2}. \quad (4.9)$$

For the coordinates of the center of the circle, we can use the fact that the center has to lie on the axis of its chord. In other words, there is a value of a parameter t such that, using the parametric equation of the axis

$$\begin{pmatrix} x_0 \\ z_0 \end{pmatrix} = \begin{pmatrix} \frac{x_1+x_2}{2} \\ \frac{z_1+z_2}{2} \end{pmatrix} + t \begin{pmatrix} \frac{z_2-z_1}{2} \\ \frac{x_1-x_2}{2} \end{pmatrix}. \quad (4.10)$$

At the same time, the center has to be in a distance of r from the nodes:

$$\begin{aligned} (x_1 - x_0)^2 + (z_1 - z_0)^2 &= r^2, \\ \left(\frac{x_1 - x_2}{2} + \frac{z_1 - z_2}{2}t \right)^2 + \left(\frac{z_1 - z_2}{2} + \frac{x_2 - x_1}{2}t \right)^2 &= r^2, \\ \left(\left(\frac{x_2 - x_1}{2} \right)^2 + \left(\frac{z_2 - z_1}{2} \right)^2 \right)t^2 + \left(\frac{x_2 - x_1}{2} \right)^2 + \left(\frac{z_2 - z_1}{2} \right)^2 - r^2 &= 0. \end{aligned} \quad (4.11)$$

²Electron tracks bend towards negative z , we need to use the upper part of the circle

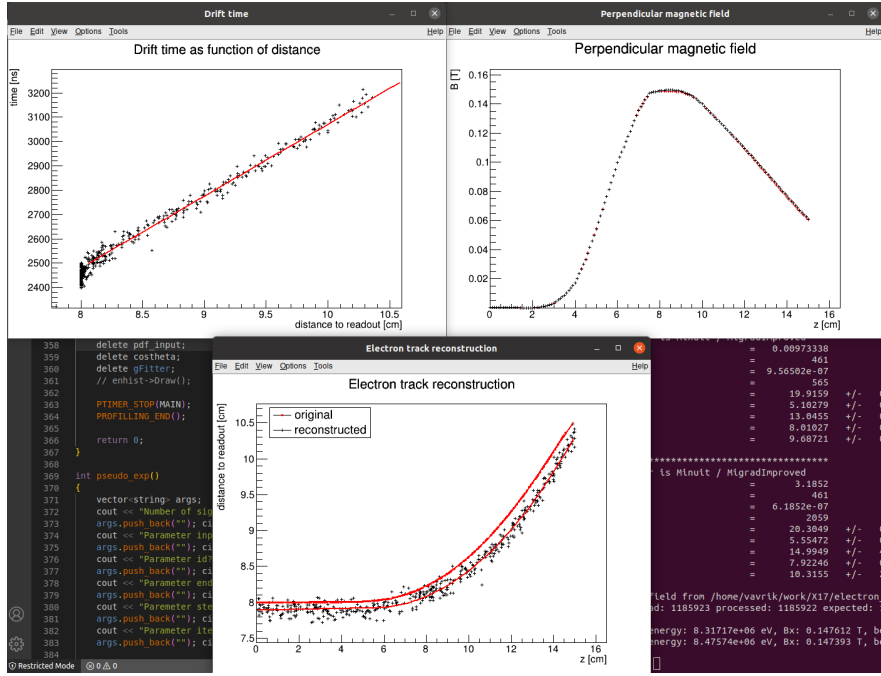


Figure 4.3: First attempt at a track reconstruction using only the drift velocity. Circle and Lines Fit in 2D. Swap for better image, correct coordinates. Bias should be described in the previous chapter, not here.

962 Since our electron track bends towards negative z and $x_2 > x_1$, we only care
963 about the solution with $t > 0$

$$t = \sqrt{\frac{r^2}{\left(\frac{x_2-x_1}{2}\right)^2 + \left(\frac{z_2-z_1}{2}\right)^2} - 1}, \quad (4.12)$$

$$x_0 = \frac{x_1 + x_2}{2} + \frac{z_2 - z_1}{2} \sqrt{\frac{r^2}{\left(\frac{x_2-x_1}{2}\right)^2 + \left(\frac{z_2-z_1}{2}\right)^2} - 1}, \quad (4.13)$$

$$z_0 = \frac{z_1 + z_2}{2} - \frac{x_2 - x_1}{2} \sqrt{\frac{r^2}{\left(\frac{x_2-x_1}{2}\right)^2 + \left(\frac{z_2-z_1}{2}\right)^2} - 1}.$$

964 The function defined in Equation 4.6 along with equations 4.8, 4.9, and 4.13
965 derived using the continuity and smoothness conditions (combined with the re-
966 lations for $z_{1,2}$) fully define our fitted function with parameters $r, x_{1,2}, z_{1,2}$. Some
967 pictures of the fit on the tested track. Results of the fit. Again, the actual fit
968 uses 8-z. Use GeoGebra schematics to generate a picture of 2D geometry.

969 4.2.2 Three-dimensional fit

970 Explain the geometry and least square method used for the 3D fit. Tested on
971 a Runge-Kutta sample, and with microscopic tracks + map simulation.

972 In three dimensions, the shape of a trajectory of a charged particle in a uniform
973 magnetic field is a cylindrical helix. Nevertheless, since we assume that the
974 field is approximately perpendicular to the particle's momentum at all times, we

will further approximate the trajectory with a circular arc (with lines attached smoothly).

We assume that the initial position $\mathbf{X}_0 = (x_0, y_0, z_0)$ and direction θ, φ (spherical angles as in Section 1.4.2) are known, since this information will be provided by TPX3 and MWPC layers. We could further refine it at the end of the current algorithm with some kind of global fit (all detector layers). The fit then has four free parameters (figure):

- the length of the first line l (as measured from the initial position),
- the radius of the circular arc r ,
- the central angle of the arc $\phi_{\max} \in [0, 2\pi]$,
- the direction of the curvature given by the angle $\alpha \in [0, 2\pi]$ (right-handed with respect to the particle direction, $\alpha = 0$ if the particle curves towards negative z in a plane given by $\hat{\mathbf{z}}$ and the direction vector).

Using these parameters, we can derive a parametrization of the whole curve. Let \mathbf{v} be the initial unit direction vector, i.e., using the spherical angles

$$\mathbf{v} = (\cos \varphi \cos \theta, \sin \varphi \cos \theta, \sin \theta)^T, \quad (4.14)$$

then we can parameterize the first line as follows:

$$\mathbf{X}_{L1}(t) = \mathbf{X}_0 + t\mathbf{v} \quad t \in [0, l]. \quad (4.15)$$

This gives us the starting point of the arc

$$\mathbf{X}_1 = \mathbf{X}_{L1}(l) = \mathbf{X}_0 + l\mathbf{v}. \quad (4.16)$$

The vector \mathbf{c}_1 that lies in the plane of curvature and points from \mathbf{X}_1 to the center of curvature can be calculated using a composition of rotations. First, we rotate \mathbf{v} to point in the $\hat{\mathbf{x}}$ direction, the normal for $\alpha = 0$ than points in the $-\hat{\mathbf{z}}$ direction, we apply the α rotation and reverse the rotations into the $\hat{\mathbf{x}}$ direction: (parameters are explained in the bullet points above)

$$\begin{aligned} \mathbf{c}_1 &= R_z(\varphi)R_y(-\theta)R_x(\alpha)R_y\left(\frac{\pi}{2}\right)R_y(\theta)R_z(-\varphi)\mathbf{v}, \\ &= R_z(\varphi)R_y(-\theta)R_x(\alpha)(-\hat{\mathbf{z}}), \\ &= \begin{pmatrix} \cos \varphi & -\sin \varphi & 0 \\ \sin \varphi & \cos \varphi & 0 \\ 0 & 0 & 1 \end{pmatrix} \begin{pmatrix} \cos \theta & 0 & -\sin \theta \\ 0 & 1 & 0 \\ \sin \theta & 0 & \cos \theta \end{pmatrix} \begin{pmatrix} 1 & 0 & 0 \\ 0 & \cos \alpha & -\sin \alpha \\ 0 & \sin \alpha & \cos \alpha \end{pmatrix} \begin{pmatrix} 0 \\ 0 \\ -1 \end{pmatrix}, \quad (4.17) \\ &= \begin{pmatrix} -\sin \alpha \sin \varphi + \cos \alpha \cos \varphi \sin \theta \\ \sin \alpha \cos \varphi + \cos \alpha \sin \varphi \sin \theta \\ -\cos \alpha \cos \theta \end{pmatrix}. \end{aligned}$$

Signs should be correct because right-handed rotation around y rotates z into x and this one is the opposite. Seems like in this part of the code θ is actually taken from the pole. Instead of the equator plane. Similarly by rotating $\hat{\mathbf{y}}$, we can get the normal vector $\mathbf{n} = \mathbf{v} \times \mathbf{c}_1$ perpendicular to the plane of the trajectory:

$$\mathbf{n} = R_z(\varphi)R_y(-\theta)R_x(\alpha)\hat{\mathbf{y}} = \begin{pmatrix} -\cos \alpha \sin \varphi - \sin \alpha \cos \varphi \sin \theta \\ \cos \alpha \cos \varphi - \sin \alpha \sin \varphi \sin \theta \\ \sin \alpha \cos \theta \end{pmatrix}. \quad (4.18)$$

1001 This allows us to express the coordinates of the center \mathbf{C} of the circular arc:

$$\mathbf{C} = \mathbf{X}_1 + r\mathbf{c}_1. \quad (4.19)$$

1002 We can then get the parametrization and the endpoint of the circular arc using
1003 Rodrigues' rotation formula: (all parameters explained in the bullet points above)

$$\begin{aligned} \mathbf{c}_2 &= \mathbf{c}_1 \cos \phi_{\max} + (\mathbf{n} \times \mathbf{c}_1) \sin \phi_{\max} + \mathbf{n}(\mathbf{n} \cdot \mathbf{c}_1)(1 - \cos \phi_{\max}), \\ &= \mathbf{c}_1 \cos \phi_{\max} - \mathbf{v} \sin \phi_{\max}, \end{aligned} \quad (4.20)$$

$$\mathbf{X}_C(\phi) = \mathbf{C} - r(\mathbf{c}_1 \cos \phi - \mathbf{v} \sin \phi) \quad \phi \in [0, \phi_{\max}], \quad (4.21)$$

$$\mathbf{X}_2 = \mathbf{X}_C(\phi_{\max}) = \mathbf{C} - r\mathbf{c}_2, \quad (4.22)$$

1004 and if we define the direction vector of the second line, we also get its parametriza-
1005 tion

$$\mathbf{w} = \mathbf{v} \cos \phi_{\max} + (\mathbf{n} \times \mathbf{v}) \sin \phi_{\max} = \mathbf{v} \cos \phi_{\max} + \mathbf{c}_1 \sin \phi_{\max}, \quad (4.23)$$

$$\mathbf{X}_{L2}(s) = \mathbf{X}_2 + s\mathbf{w} \quad s \in [0, \infty). \quad (4.24)$$

1006 The fit is performed as a (weighted) least square minimization (MIGRAD
1007 ROOT), therefore we need to derive the distance of any point \mathbf{P} to the fitted
1008 curve. For the first line, we simply compute the parameter value of the closest
1009 point on the line:

$$\begin{aligned} t_P &= \mathbf{v} \cdot (\mathbf{P} - \mathbf{X}_1), \\ d_{P1} &= \|\mathbf{P} - \mathbf{X}_{L1}(t_P)\|. \end{aligned} \quad (4.25)$$

1010 If the parameter value is outside of its bounds defined above, we take the bound-
1011 ary value instead. The distance to the second line is computed likewise. For
1012 the circular arc (specific circular arc in the fit), we find the closest point (on the
1013 arc) by projecting the center connecting line onto the arc plane:

$$\mathbf{X}_{PC} = \mathbf{X}_C + r \frac{(\mathbf{P} - \mathbf{X}_C) - (\mathbf{n} \cdot (\mathbf{P} - \mathbf{X}_C))\mathbf{n}}{\|(\mathbf{P} - \mathbf{X}_C) - (\mathbf{n} \cdot (\mathbf{P} - \mathbf{X}_C))\mathbf{n}\|}, \quad (4.26)$$

$$d_{PC} = \|\mathbf{P} - \mathbf{X}_{PC}\| \quad (4.27)$$

1014 Potential problem in the implementation – might not be correctly handling ϕ
1015 out of bounds, the distance could be sometimes underestimated because of this.

1016 The shortest distance out of d_{P1}, d_{PC}, d_{P2} is then taken as the distance to the curve. When
1017 calculating energy with the average field, only the arc is considered. Middle field
1018 in the current implementation taken in the middle x plane (intersection with
1019 the curve). TVirtualFitter+MIGRAD, maximal num of iterations, toleration.
1020 Different uncertainties in x, y, z not taken into account.

1021 Fit details (parameter bounds, initial setting).

1022 4.2.3 Testing on a Runge-Kutta sample

1023 The three dimensional circle and lines fit was tested on a sample of Runge-Kutta
1024 tracks with randomized parameters described in Section 2.2.1. These tracks of
1025 primary electrons and positrons consist of points calculated with the RK4 algo-
1026 rithm for a given proper time step (step can be adjusted by dividing by the gamma
1027 factor → detector time). Fitting with circle only was also partially implemented
1028 (didn't work but could be fixed/tuned).

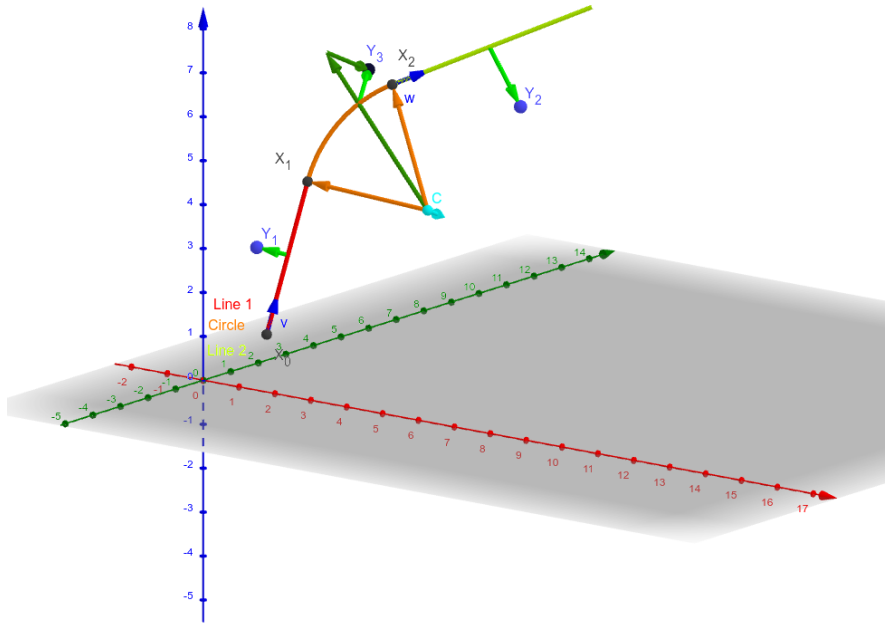


Figure 4.4: Circle and Lines Fit 3D geometry. Swap for better image.

1029 4.3 Runge-Kutta Fit

1030 The Runge-Kutta fit uses the Runge-Kutta 4th order (RK4) numerical integration
 1031 of the equation of motion (see Section 2.2) to find the best values of the track
 1032 parameters – the track origin, initial velocity direction and the kinetic energy. In
 1033 order to speed up the energy reconstruction, an initial guess of these parameters
 1034 can be obtained from the 3D circle fit described in the previous section. Fur-
 1035 thermore, assuming we know the track origin and orientation, we can perform
 1036 a single parameter fit of the kinetic energy (**do some profiling and show that it is**
 1037 **faster – below in the microscopic testing**).

1038 The fit is performed as a least square minimization of the (weighted) distances
 1039 of the track points (true ionization vertices from the simulation or reconstructed
 1040 points). The simulated RK4 track consists of line segments with known endpoints,
 1041 therefore we can calculate the distance of a point from this segment analogically
 1042 to Equation 4.25 with \mathbf{v} given as a unit vector in the direction of the segment.

1043 We need to find the segment with the lowest distance. We assume, that
 1044 the distance $d_{\mathbf{P}}(\tau)$ of a point \mathbf{P} to the point on the track $\mathbf{X}(\tau)$ has a single
 1045 minimum (local and global), no local maximum (except the interval endpoints)
 1046 and no saddle point

$$\exists! \tau_{\min} \in [0, \tau_N]: (\forall \tau \in [0, \tau_N]: d_{\mathbf{P}}(\tau) \geq d_{\mathbf{P}}(\tau_{\min})) \vee \frac{dd_{\mathbf{P}}}{d\tau}(\tau_{\min}) = 0, \quad (4.28)$$

1047 where N is the number of RK4 steps. This is a reasonable assumption for a track
 1048 with an approximate shape of a circular arc with a radius r , since the distance d
 1049 from a point \mathbf{C} on the corresponding circle of a point \mathbf{P} offset by a from the arc
 1050 plane and by b from the arc's center when projected on its plane is given by the

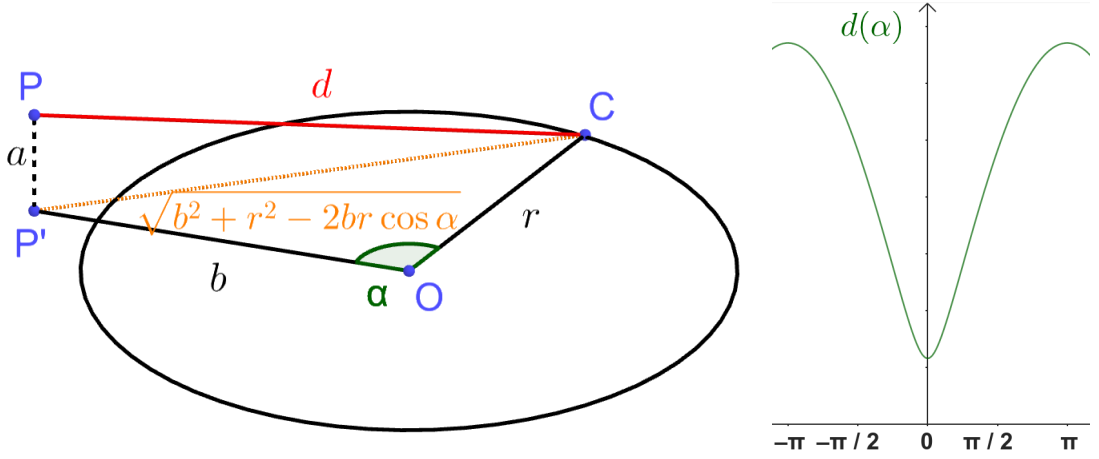


Figure 4.5: Demonstration of the convexity of the distance function $d(\alpha)$ for a circular track (see Equation 4.29).

1051 law of cosines:

$$d^2 = a^2 + b^2 + r^2 - 2br \cos \alpha, \quad (4.29)$$

1052 where α is the angle between points \mathbf{C} and \mathbf{P} as seen from the center of the track
1053 (see Fig. 4.5). This function is strictly convex for $\alpha \in (-\frac{\pi}{2}, \frac{\pi}{2})$ and in our case,
1054 the center of the arc lies outside of the detector and α is restricted to a small
1055 interval around zero (especially considering that the initial guess should make the
1056 fitted trajectory reasonably close to any relevant point, in the worst-case scenario,
1057 the distance is overestimated which should keep the fit from converging to such
1058 solutions).

1059 In a more general case, if we consider the vector $\mathbf{a}(\tau) = \mathbf{P} - \mathbf{X}(\tau)$ whose size
1060 is $\|\mathbf{a}(\tau)\| = d_{\mathbf{P}}(\tau)$, then we get

$$2d_{\mathbf{P}} \frac{dd_{\mathbf{P}}}{d\tau} = \frac{dd_{\mathbf{P}}^2}{d\tau} = \frac{d}{d\tau} \sum_i a_i^2 = 2 \sum_i a_i \frac{da_i}{d\tau} = 2\mathbf{a} \cdot \frac{d\mathbf{a}}{d\tau} = -2\mathbf{a} \cdot \frac{d\mathbf{X}}{d\tau}, \quad (4.30)$$

1061 therefore for the derivative of $d_{\mathbf{P}}(\tau)$ to be zero, $\mathbf{a}(\tau)$ has to be perpendicular
1062 to the tangent of the track. In 3D, for a given $\mathbf{X}(\tau)$, this condition restricts \mathbf{P}
1063 to a plane. This means that for a curving track we can find a point \mathbf{P} for any
1064 two points $\mathbf{X}(\tau), \mathbf{X}(\sigma)$ with non-parallel tangents that has $\frac{dd_{\mathbf{P}}}{d\tau}(\tau) = \frac{dd_{\mathbf{P}}}{d\tau}(\sigma) =$
1065 $= 0$, which violates the assumption 4.28. If we have a circle-and-lines track as
1066 described in the previous sections, such a point has to lie outside of the circular
1067 sector given by the arc.

1068 For a planar track, the envelope of all its normals is the evolute of the curve
1069 (i.e., the set of centers of all its osculating circles). If the track has a monotonous
1070 tangent angle

$$\alpha(\tau) = \text{atan} \frac{\frac{dX_2}{d\tau}}{\frac{dX_1}{d\tau}} \quad (4.31)$$

1071 with minimal and maximal α differing by less than π (i.e., the track changes
1072 direction by less than 180°), then all intersections of the track's normals must lie
1073 on the side of the evolute closer to the track (not obvious?, sometimes the sides
1074 are opposite?). At the same time, the intersection must lie in the half planes
1075 given by the normals at the beginning and the end of the curve and pointing

1076 away from the curve. Together, these three boundaries define a closed shape that
1077 will lie outside of the OFTPC for a typical track in our detector.

1078 With the assumption 4.28, we can find the segment on the RK4 track with
1079 the lowest distance to a given point \mathbf{P} using a binary search algorithm. Let
1080 the distance of the point from the n -th vertex be $d_{\mathbf{P},n}$. Then the difference
1081 $\Delta d_{\mathbf{P},n} = d_{\mathbf{P},n} - d_{\mathbf{P},n-1}$ satisfies

$$\begin{aligned}\Delta d_{\mathbf{P},n} &< 0 \quad \forall n \text{ such that } \tau_n < \tau_{\min}, \\ \Delta d_{\mathbf{P},n} &> 0 \quad \forall n \text{ such that } \tau_{n-1} > \tau_{\min}.\end{aligned}\tag{4.32}$$

1082 Therefore, we can search for the segment containing $d_{\mathbf{P},\min}$ with binary search
1083 starting with $\Delta d_{\mathbf{P},1}$ and $\Delta d_{\mathbf{P},N}$, then calculate the difference $\Delta d_{\mathbf{P},m}$ for the middle
1084 index $m = \left\lfloor \frac{N+1}{2} \right\rfloor$. If $\Delta d_{\mathbf{P},m} > 0$ (minor bug in the implementation – if the
1085 value for the maximal index is negative, it shouldn't change anything), we can
1086 replace the higher index with m , otherwise we replace the lower index. The search
1087 stops when the difference between the minimal and maximal index is one. Would
1088 it be better if they were the same (maybe not)? Then the minimal value is
1089 $d_{\mathbf{P},n-1}$ or $d_{\mathbf{P},N}$ and we can take the minimum of the distances from the two
1090 segments connected to $n-1$. Currently taking the maximal index (and starting
1091 at $N-2$ maximal index $\leftrightarrow N-1$ -th point), this should be equivalent, since either
1092 $\Delta d_{\mathbf{P},\max} > 0$ (in the code is equivalent to max-1 here) or we are at $N-1$. The
1093 minimum of the two distances still taken.

1094 Same details with MIGRAD etc. as previously.

1095 4.3.1 Testing on a microscopic sample

1096 The Runge-Kutta fit together with the 3D circle-and-lines pre-fit was tested
1097 on a sample of tracks simulated using the microscopic simulation described in
1098 Section 2.1. At first, few tracks with randomized initial parameters (same as
1099 the Runge-Kutta sample in Section 2.2.1) were generated for preliminary testing.
1100 Later, a sample with a grid-like distribution of track parameters was generated
1101 (see Section 2.1.2 for details).

1102 Initial parameters of the HEED track (also should be in the first testing track
1103 → subsection of microsim?). Initial parameters set in the circle fit (if electron set
1104 alpha one way, otherwise other way) and parameter bounds.

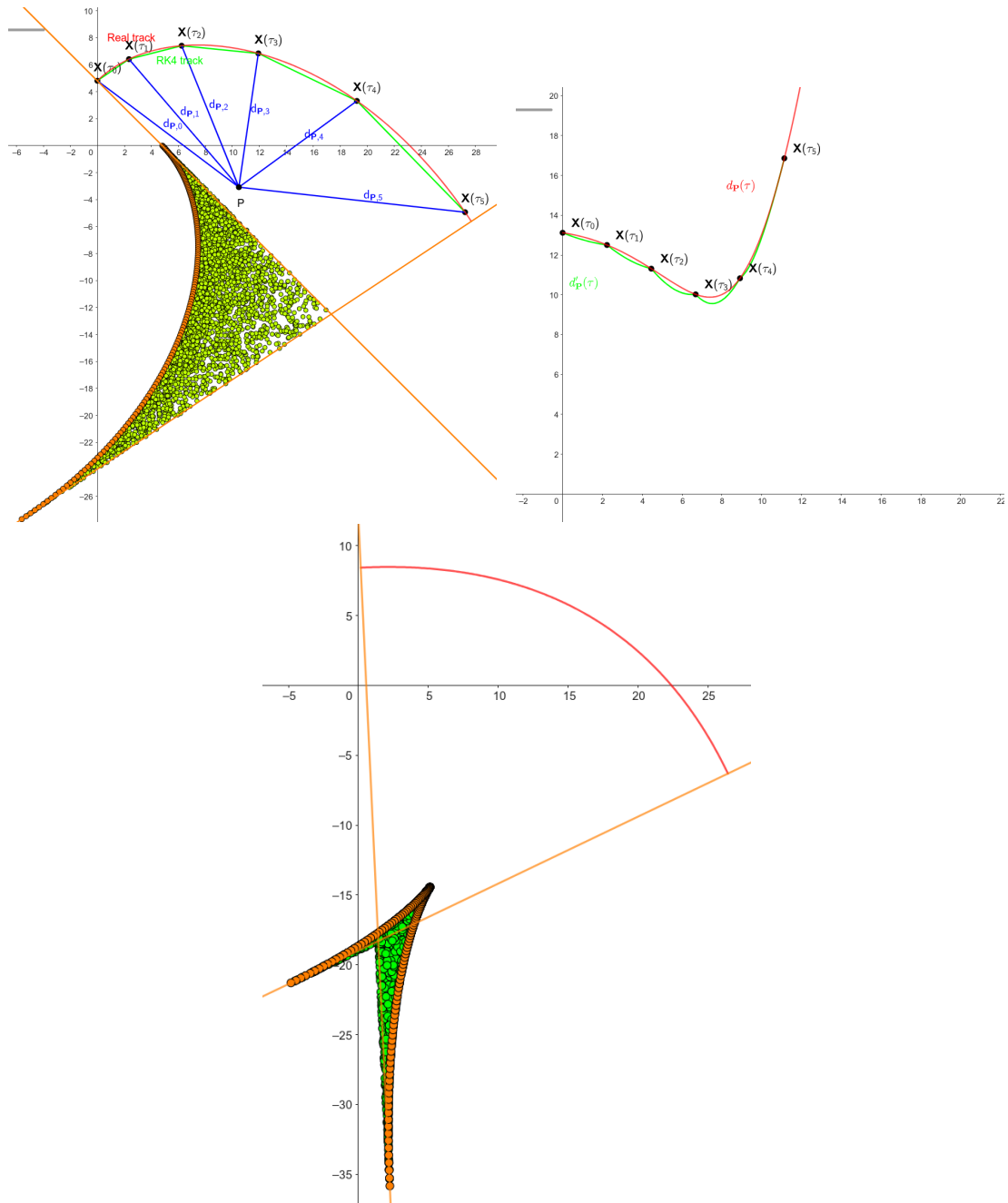


Figure 4.6: some provisional figures

1105 Conclusion

1106 Here or at the end of each section. Something about the future of this work?

1107

1108 Notes

1109 General notes about the thesis:

- 1110 • Check that all of the classes and other code are marked the same way in
- 1111 the text. I used italics somewhere, could use different font for this instead.
- 1112 • Check unbreakable space in front of articles. Remove excessive article usage
- 1113 with proper nouns.
- 1114 • Currently using margins for single-sided printing (bigger on the left side).
- 1115 • Check that present tense is used
- 1116 • Active vs passive voice usage
- 1117 • American English quotation marks (") instead of British English (').
- 1118 • Some of the overfull hbox warnings might change if duplex printing is used
- 1119 (they generate black rectangles on the edge of the page), leaving them be
- 1120 for now
- 1121 • Check nobreakdash usage (is it always necessary)
- 1122 • Check capitalized references (e.g., Figure, Section, Equation)
- 1123 • Check $\backslash(...\backslash)$ math mode instead of $\$...$$. (actually unlike $\backslash[...\backslash]$ math mode,
- 1124 there is apparently no real benefit to this clumsy syntax)
- 1125 • Use siunitx package to ensure correct formatting, physics package for derivatives.
- 1127 • Check other stuff that's written in the MFF UK template. Apparently it
- 1128 has since been updated and there are some differences (check for them).
- 1129 • Check correct subscripts in equation (italics vs no italics)
- 1130 • Consistent bold marking of points/vectors
- 1131 • Correct footnotes (capital letters, etc.).
- 1132 • Might have to mention GeoGebra as per the non-commercial license agree-
- 1133 ment (Made with GeoGebra®) – maybe put it into acknowledgments next
- 1134 to the MetaCentrum credit? And list all of the figures where GeoGebra was
- 1135 used?
- 1136 • Maybe make some section outside of References specifically for literature?
- 1137 (such as the old CERN TPC review, ATOMKI review is currently not
- 1138 mentioned, not sure if some Wikipedia articles should get a mention or how
- 1139 do these things work)
- 1140 • Consistent use of `bm` vs `mathbf`

- Consistent use of $\bar{\mathcal{M}}$ instead of \mathcal{M} when talking about the map of the means (so most of the time)
 - Proper equation numbering when deriving a relation
 - Hugo should be mentioned somewhere in the title pages probably?
 - Consistent itemize/enumerate style (namely spacing) that looks good (ideally set by some macro? maybe the new MFF UK template will solve this?)
 - Consistent gas mixture notation (e.g., 90:10 Ar:CO₂). Maybe mention at the beginning that it is a molar ratio.
 - Labels of figures and tables – maybe in bold? Abbreviated?
 - Check graph labels, make them bigger if needed.
 - "The map" can be viewed as a mapping between spaces or just as a coordinate transform.
 - Maybe switch to cleverref.
 - siunitx qty not SI
- 1155 Random notes:
- Terminology consistency – ionization/primary/secondary electrons
 - Consistent TPC vs OFTPC acronym usage in the text or individual chapters.
 - Only electrons that start and end in the sector closer than 0.5 cm are used for reconstruction (newest version).
 - Attachment, Penning transfer and secondary ionization not considered in the microscopic simulation.
 - Suspicious artifacts of trilinear interpolation in Fig. 1.8. **Fixed – integers instead of doubles in the implementation, influenced reconstruction SIGNIFICANTLY (but not simulation).**
 - Profiling of the reconstruction!!!! Find out what's taking the most time (probably Runge-Kutta integration which the fit calls a lot). Could gradually decrease the step size to refine the fit instead of making it small right away (arbitrarily small – the effect of this was never tested). This could take some time to do properly (find a profiler or make profiling macros).
 - Slow drift velocity good for z reconstruction, too low leads to recombination
 - Could add link to the GitHub repository, mention CMake? Details about simulating on MetaCentrum?
 - The first used track had 8 MeV momentum $p = \gamma mv$ (not kinetic energy $E_{\text{kin}} = (\gamma - 1)mc^2 = \sqrt{p^2c^2 + m^2c^4} - mc^2 \approx 7.5$ MeV)
 - Maybe cite Garfield++ user manual instead?
 - Using TRandom3 for random number generation.
 - Does the RK fit error correlate with the actual error?

- 1179 • Some Garfield settings in micro track generation probably not mentioned

1180

Future

1181 Things planned for the future:

- 1182 • Testing the reconstruction algorithm by measuring real particles with a known energy distribution.
- 1184 • The **Fast Simulation with Ionization Electron Map** is planned for the future. It will use the HEED program [32] to simulate the primary particle and the Ionization Electron Map (see Section 3.2) to simulate the drift of secondary electrons. It should be significantly faster than the Microscopic Simulation but offer comparable precision since it will rely on an already simulated drift map. (Primary track simulated in HEED. Readout parameters by interpolating the map. Diffusion from the map for randomization.)
- 1191 • Account for GEM, delta electrons, ...
- 1192 • Likelihood approach instead of least squares (if it improves the reconstruction significantly), we should at least use a better method than taking the center of the TPC bin.
- 1195 • More detailed electric field simulation (if needed, GEM will have more complex field, some irregularities in the field should be considered)
- 1197 • Account for the triggering in MWPC/TPX3 (particle travels from TPX3 to MWPC basically immediately – fraction of a nanosecond so there should be no significant difference)

1200

1201

Likelihood - inverse map

1202 If we wanted to further improve this procedure, taking into account the whole
 1203 map \mathcal{M} , we could make an "inverse map" from \mathcal{R} to distributions on \mathcal{D} . We could
 1204 achieve this by taking the normalized probability density of an electron with initial
 1205 coordinates (x, y, z) having readout coordinates (x', y', t) . If we fix (x', y', t) , we
 1206 get an unnormalized probability density $f(x, y, z) = \mathcal{M}_{(x,y,z)}(x', y', t)$ (assuming
 1207 that all initial coordinates are a priori equally likely). This could potentially
 1208 improve the discrete reconstruction if we take the mean value of this probability
 1209 density across the pad and time bin

$$f_{\text{pad, bin}}(x, y, z) = \frac{1}{A_{\text{pad}} \Delta t_{\text{bin}}} \int_{\text{pad, bin}} \mathcal{M}_{(x,y,z)}(x', y', t) dx' dy' dt \quad (4.33)$$

1210 and using it for a likelihood fit instead of using least squares. This still assumes
 1211 that all initial coordinates are equally likely which is clearly not the case for
 1212 a primary particle track. In the future, we could even use the fast track simulation
 1213 with the map (should be possible to make around 1000 tracks per minute per core
 1214 with current settings), create a big set of tracks with reasonable parameters and
 1215 use these to get an approximation of the probability distribution of the detector

1216 response. Some approximations would be necessary when interpreting the data to
1217 decrease the degrees of freedom of this distribution (we would have to pick a set of
1218 parameters and assume that some of them are independent). This could give us
1219 an idea about the best achievable resolution (how significantly will the detector
1220 response differ for a given change in energy). If the difference is significant, we
1221 could try to further improve the likelihood fit.

Bibliography

1. *Garfield++* [<https://garfieldpp.web.cern.ch/garfieldpp/>]. [N.d.]. Accessed: 2023-05-18.
2. BRUN, Rene; RADEMAKERS, Fons. Root — An Object Oriented Data Analysis Framework. *Nucl. Instrum. Methods Phys. Res. Sect. A: Accel. Spectrom. Detect. Assoc. Equip.* 1997, vol. 389, no. 1–2, pp. 81–86. Available from DOI: 10.1016/s0168-9002(97)00048-x. Proceedings AIHENP'96 Workshop, Lausanne, Sep. 1996, See also <https://root.cern/>, Paper published in the Linux Journal, Issue 51, July 1998.
3. *About MetaCentrum* [<https://metavo.metacentrum.cz/en/about/index.html>]. 2023. Accessed: 2024-11-27.
4. ROSE, M. E. Internal Pair Formation. *Phys. Rev.* 1949, vol. 76, pp. 678–681. Available from DOI: 10.1103/PhysRev.76.678.
5. ESSIG, R. et al. *Dark Sectors and New, Light, Weakly-Coupled Particles*. 2013. Available from arXiv: 1311.0029 [hep-ph].
6. DE BOER, F.W.N. et al. A deviation in internal pair conversion. *Phys. Lett. B*. 1996, vol. 388, no. 2, pp. 235–240. ISSN 0370-2693. Available from DOI: [https://doi.org/10.1016/S0370-2693\(96\)01311-1](https://doi.org/10.1016/S0370-2693(96)01311-1).
7. BOER, F W N de et al. Excess in nuclear pairs near 9 MeV/ invariant mass. *J. Phys. G: Nucl. Part. Phys.* 1997, vol. 23, no. 11, p. L85. Available from DOI: 10.1088/0954-3899/23/11/001.
8. BOER, F W N de et al. Further search for a neutral boson with a mass around 9 MeV/c². *J. Phys. G: Nucl. Part. Phys.* 2001, vol. 27, no. 4, p. L29. Available from DOI: 10.1088/0954-3899/27/4/102.
9. VITÉZ, Attila et al. Anomalous Internal Pair Creation in ⁸Be as a Signature of the Decay of a New Particle. *Acta Phys. Pol. B - ACTA PHYS POL B*. 2008, vol. 39, p. 483.
10. KRASZNAHORKAY, A. et al. Searching for a light neutral axial-vector boson in isoscalar nuclear transitions. *Frascati Phys. Ser.* 2012, vol. 56, p. 86.
11. KRASZNAHORKAY, A. J. et al. Observation of Anomalous Internal Pair Creation in ⁸Be: A Possible Indication of a Light, Neutral Boson. *Phys. Rev. Lett.* 2016, vol. 116, no. 4. ISSN 1079-7114. Available from DOI: 10.1103/physrevlett.116.042501.
12. TILLEY, D.R. et al. Energy levels of light nuclei A=8,9,10. *Nucl. Phys. A*. 2004, vol. 745, no. 3, pp. 155–362. ISSN 0375-9474. Available from DOI: <https://doi.org/10.1016/j.nuclphysa.2004.09.059>.
13. SAS, N. J. et al. *Observation of the X17 anomaly in the ⁷Li(p,e⁺e⁻)⁸Be direct proton-capture reaction*. 2022. Available from arXiv: 2205.07744 [nucl-ex].
14. KRASZNAHORKAY, A. J. et al. New anomaly observed in ⁴He supports the existence of the hypothetical X17 particle. *Phys. Rev. C*. 2021, vol. 104, no. 4. ISSN 2469-9993. Available from DOI: 10.1103/physrevc.104.044003.

- 1264 15. TILLEY, D.R. et al. Energy levels of light nuclei A = 4. *Nucl. Phys. A*.
1265 1992, vol. 541, no. 1, pp. 1–104. ISSN 0375-9474. Available from DOI: [https://doi.org/10.1016/0375-9474\(92\)90635-W](https://doi.org/10.1016/0375-9474(92)90635-W).
- 1266
- 1267 16. KRASZNAHORKAY, A. J. et al. New anomaly observed in ^{12}C supports the
1268 existence and the vector character of the hypothetical X17 boson. *Phys. Rev.*
1269 *C*. 2022, vol. 106, p. L061601. Available from DOI: 10.1103/PhysRevC.106.
1270 L061601.
- 1271 17. AJZENBERG-SELOVE, F. Energy levels of light nuclei A = 11,12. *Nucl. Phys.*
1272 *A*. 1990, vol. 506, no. 1, pp. 1–158. ISSN 0375-9474. Available from DOI:
1273 [https://doi.org/10.1016/0375-9474\(90\)90271-M](https://doi.org/10.1016/0375-9474(90)90271-M).
- 1274 18. KÁLMÁN, Péter; KESZTHELYI, Tamás. Anomalous internal pair creation.
1275 *The Eur. Phys. J. A*. 2020, vol. 56. Available from DOI: 10.1140/epja/
1276 s10050-020-00202-z.
- 1277 19. ALEKSEJEVS, A. et al. *A Standard Model Explanation for the "ATOMKI*
1278 *Anomaly*". 2021. Available from arXiv: 2102.01127 [hep-ph].
- 1279 20. FENG, Jonathan L. et al. Protophobic Fifth-Force Interpretation of the Ob-
1280 served Anomaly in ^8Be Nuclear Transitions. *Phys. Rev. Lett.* 2016, vol. 117,
1281 p. 071803. Available from DOI: 10.1103/PhysRevLett.117.071803.
- 1282 21. ANH, Tran The et al. Checking the 8Be Anomaly with a Two-Arm Electron
1283 Positron Pair Spectrometer. *Universe*. 2024, vol. 10, no. 4, p. 168. ISSN 2218-
1284 1997. Available from DOI: 10.3390/universe10040168.
- 1285 22. ABRAAMYAN, Kh. U. et al. *Observation of structures at ~ 17 and ~ 38 MeV/c 2*
1286 *in the $\gamma\gamma$ invariant mass spectra in pC, dC, and dCu collisions at p_{lab} of a*
1287 *few GeV/c per nucleon*. 2023. Available from arXiv: 2311.18632 [hep-ex].
- 1288 23. THE MEG II COLLABORATION et al. *Search for the X17 particle in $^7\text{Li}(p, e^+e^-)^8\text{Be}$*
1289 *processes with the MEG II detector*. 2024. Available from arXiv: 2411.07994
1290 [nucl-ex].
- 1291 24. ABED ABUD, Adam et al. A Gaseous Argon-Based Near Detector to En-
1292 hance the Physics Capabilities of DUNE. 2022. Available from DOI: 10.
1293 48550/arXiv.2203.06281.
- 1294 25. LOKEN, Stewart C. et al. Performance of the Signal Processing System for
1295 the Time Projection Chamber. *IEEE Trans. on Nucl. Sci.* 1983, vol. 30, no.
1296 1, pp. 162–166. Available from DOI: 10.1109/TNS.1983.4332243.
- 1297 26. ADAMOVÁ, D. et al. The CERES/NA45 radial drift Time Projection Cham-
1298 ber. *Nucl. Instrum. Methods Phys. Res. Sect. A: Accel. Spectrom. Detect.*
1299 *Assoc. Equip.* 2008, vol. 593, no. 3, pp. 203–231. ISSN 0168-9002. Available
1300 from DOI: 10.1016/j.nima.2008.04.056.
- 1301 27. NAVAS, S. et al. Review of particle physics. *Phys. Rev. D*. 2024, vol. 110,
1302 no. 3, p. 030001. Available from DOI: 10.1103/PhysRevD.110.030001.
- 1303 28. HILDÉN, T. et al. Optical quality assurance of GEM foils. *Nucl. Instrum.*
1304 *Methods Phys. Res. Sect. A: Accel. Spectrom. Detect. Assoc. Equip.* 2015,
1305 vol. 770, pp. 113–122. ISSN 0168-9002. Available from DOI: 10.1016/j.
1306 nima.2014.10.015.

- 1307 29. AHMED, Misbah Uddin. *Simulation of the electron and ion movement through*■
1308 *a 4-GEM stack*. 2021. Institut für Kernphysik.
- 1309 30. MARMELAD. *3D interpolation2.svg*. 2025. Available also from: https://commons.wikimedia.org/wiki/File:3D_interpolation2.svg. Licensed
1310 under CC BY-SA 3.0 (<https://creativecommons.org/licenses/by-sa/3.0/legalcode>). Accessed: 9-April-2025.
- 1311 31. CMGLEE. *Trilinear interpolation visualisation*. 2025. Available also from:
1312 https://commons.wikimedia.org/wiki/File:Trilinear_interpolation_visualisation.svg. Licensed under CC BY-SA 3.0 (<https://creativecommons.org/licenses/by-sa/3.0/legalcode>). Accessed: 26-March-2025.
- 1313 32. SMIRNOV, I.B. Modeling of ionization produced by fast charged particles in
1314 gases. *Nucl. Instrum. Methods Phys. Res. Sect. A: Accel. Spectrom. Detect.*
1315 *Assoc. Equip.* 2005, vol. 554, no. 1, pp. 474–493. ISSN 0168-9002. Available
1316 from DOI: <https://doi.org/10.1016/j.nima.2005.08.064>.

1321 **Acknowledgments:** Computational resources were provided by the e-INFRA
1322 CZ project (ID:90254), supported by the Ministry of Education, Youth and Sports
1323 of the Czech Republic. **Figures that were drawn with GeoGebra. Maybe grant?**

1324 List of Figures

1325 0.1	The ATOMKI anomalous IPC measured for different nuclei.	5
1326 0.2	Results from the Hanoi spectrometer – angular e^+e^- pair correlations measured in the ${}^7\text{Li}(p, e^+e^-){}^8\text{Be}$ reaction at $E_p = 1225$ keV [21].	6
1327 0.3	Results from the MEG II experiments – angular correlation of e^+e^- pairs with $E_{\text{sum}} \in [16, 20]$ MeV measured in the ${}^7\text{Li}(p, e^+e^-){}^8\text{Be}$ reaction with proton beam energies 500 and 1080 keV. The 500 keV dataset is fitted with Monte Carlo of both the IPC deexcitation and the EPC produced by gammas [23].	7
1328 0.4	Schematics of the detector at the Van der Graaff facility at IEAP CTU (ref).	7
1329 1.1	Particle identification in the PEP-4 TPC at SLAC based on the energy loss per distance $\frac{dE}{dx}$ in the 80:20 Ar:CH ₄ filling at 8.5 atm pressure [24]. The reference doesn't point to the original PEP-4 article because this adapted version of the original picture that they used in the DUNE article looks better.	9
1330 1.2	Schematic view of the PEP-4 TPC [25]. A charged particle produced in a collision in the beam pipe creates a spiral ionization track in the magnetic field. The central cathode then accelerates ionization electrons towards the endcap anode wires where they are multiplied and read out.	12
1331 1.3	Gas Electron Multiplier (GEM).	14
1332 1.4	Garfield simulation of an avalanche in a GEM hole [29]. An incoming electron (orange) is accelerated in the strong electric field of the GEM and causes further ionization multiplying the number of free electrons (orange). Most of the produced cations (red) are captured by the GEM cathode.	14
1333 1.5	MICRO-MEsh GAseous Structure (Micromegas) [27].	15
1334 1.6	Schematics of the first sector OFTPC with detector space coordinates.	17
1335 1.7	Pad layout of the OFTPC and its parameters. Pads 102, 124 and 127 are irregular, the rest has the same dimensions.	18
1336 1.8	Magnetic field simulation results. The OFTPC volume and the vacuum tube are marked with black lines, the magnets are marked with red lines. The coordinates of the magnets from the CAD drawing seem to be 9/10 of the ones from the magnetic simulation (confirm and fix).	19
1337 1.9	Visualization of trilinear interpolation as a composition of linear interpolations (inspired by [30]). We want to interpolate the value in the red point C. First we interpolate between the four pairs of blue points sharing the last two indices along the x-axis (Eq. 1.15), then between the two pairs of the resulting green points along the y-axis (Eq. 1.16) and finally between the two resulting orange points along the z-axis to get the final red value (Eq. 1.17).	20

1367	1.10 Geometric interpretation of trilinear interpolation as expressed in Equation 1.19. The colored dots represent the values in given points and the colored boxes represent the volume in the opposite corner by which the corresponding values are multiplied. The black dot represents the interpolated value which is multiplied by the entire volume [31].	21
1373	1.2.1 Comparison of drift lines for two different gas mixtures 90:10 and 70:30 Ar:CO ₂ . The electron track is marked in black, the drift lines of the ionization electrons are marked in orange. In this example, we assume a larger OFTPC volume with readout at $z = 8$ cm.	24
1377	1.2.2 A visualization of a set of tracks from the grid-like testing sample with the same kinetic energy.	25
1379	1.2.3 A comparison of the HEED track from the microscopic simulation in Section 2.1.1 with a Runge-Kutta track with the same initial parameters and $\tau_{\text{step}} = 0.1$ ps (reducing the step further doesn't make a visible difference). In the view of the tracks on the left, the distance of the HEED ionization electrons from the RK4 track is exaggerated 1000 \times . On the right, the dependence of the HEED electrons residuals (i.e., their shortest distance to the RK4 track) on their z -coordinate is shown. The images look the same even for 100,000x smaller step, so the residuals are a result of something that HEED does (maybe a different interpolation technique for the magnetic field? the pattern looks similar for two different tracks so it can't be scattering).	27
1391	2.3.1 Linear fit of the drift time t dependence on the distance to the readout $d_r = 8$ cm – z for the ionization electrons in 90:10 (left) and 70:30 (right) Ar:CO ₂ gas composition. Only electrons inside the TPC (red) are fitted. The parameters are $v_d = 3.39$ cm/ μ s, $d_0 = -0.41$ cm for 90:10, and $v_d = 0.939$ cm/ μ s, $d_0 = -0.11$ cm for 70:30 Ar:CO ₂	29
1397	2.3.2 Reconstruction (black) of the starting position of ionization elec- trons (red) using parameters obtained from the fit (Fig. 3.1). Two gas compositions 90:10 (left) and 70:30 Ar:CO ₂ (right) are compared.	30
1400	2.3.3 Comparison of residuals (i.e., the distance from the reconstructed point to the simulated ionization electron starting point) depen- dence on x for two gas mixtures 90:10 (red) and 70:30 Ar:CO ₂ (blue).	30
1404	2.3.4 A 3D visualization of the mapping of means $\overline{\mathcal{M}}$ for the 90:10 Ar:CO ₂ gas. A regular grid \mathbb{G} with $l = 1$ cm in the detector space is mapped to an irregular grid $\mathbb{G}^{-1} \equiv \overline{\mathcal{M}}(\mathbb{G})$ in the readout space.	31
1407	2.3.5 A test of the 90:10 Ar:CO ₂ map simulation with spacing $l = 1.5$ cm. The resulting drift lines of evenly spaced electrons are displayed in orange.	32
1410	2.3.6 Dependence of the drift times of the simulated map $\overline{\mathcal{M}}$ on the z -coordinate. Two gas mixtures 90:10 (left) and 70:30 Ar:CO ₂ (right) are compared. The spread is caused by varying Lorentz angles.	33

1414	3.7	The $x't$ projection of the $\mathcal{M}(\mathbb{G}_{y=0})$ mapping of a part of the regular grid \mathbb{G} . The means $\overline{\mathcal{M}}(\mathbb{G}_{y=0})$ are marked with red crosses, and the diffusion error is denoted by black 95% confidence error ellipses computed from the diagonalized covariance matrices $\mathcal{M}_\Sigma(\mathbb{G}_{y=0})$. Two gas mixtures 90:10 (left) and 70:30 Ar:CO ₂ (right) are compared. The first mixture shows differences of t for electrons with same initial z but different initial x . For the second mixture, these differences are negligible in comparison with the diffusion.	33
1422	3.8	The regular grid \mathbb{G} projected by the mapping $\overline{\mathcal{M}}$ from the detector space onto the $x'y'$ plane (t is not plotted). Layers with lower z -coordinate (i.e., further away from the readout) are displayed with darker colors. The OFTPC volume is marked with black lines. Two gas mixtures 90:10 (left) and 70:30 Ar:CO ₂ (right) are compared.	34
1428	3.9	The $\mathcal{M}(\mathbb{G}_{-8})$ mapping of the bottom ($z = -8$ cm) layer \mathbb{G}_{-8} of the regular grid $\mathbb{G} \subset \mathcal{D}$. It includes both the mapping of means $\overline{\mathcal{M}}$ and of covariances \mathcal{M}_Σ . Individual electrons from the map simulation are marked with red dots. Two gas mixtures 90:10 (left) and 70:30 Ar:CO ₂ (right) are compared.	34
1433	3.10	The readout coordinate x' for points on the grid $\mathbb{G}_{y=0}$ plotted against their initial coordinate z . The means are marked with red crosses, the diffusion in x' is denoted by standard error bars. Two gas mixtures 90:10 (left) and 70:30 Ar:CO ₂ (right) are compared.	35
1437	3.11	Example reconstruction with the map. Swap for better image, correct coordinates.	36
1439	3.12	Selection of the points for interpolation. Create better images; use the explanation interpolation vs. extrapolation strange property. Solution 2 probably does not make much sense.	39
1442	4.1	Example of a fitted reconstructed track. Swap for better image.	41
1443	4.2	First attempt at a track reconstruction using only the drift velocity. Spline energy reconstruction attempt. Swap for better image(s) – subfigure environment, correct coordinates.	43
1446	4.3	First attempt at a track reconstruction using only the drift velocity. Circle and Lines Fit in 2D. Swap for better image, correct coordinates. Bias should be described in the previous chapter, not here.	45
1450	4.4	Circle and Lines Fit 3D geometry. Swap for better image.	48
1451	4.5	Demonstration of the convexity of the distance function $d(\alpha)$ for a circular track (see Equation 4.29).	49
1453	4.6	some provisional figures	51

List of Tables

1454	3.1 Comparison of parameters of two map simulations.	32
------	--	----

1455

¹⁴⁵⁶ List of Abbreviations

- ¹⁴⁵⁷ **GEM** Gas Electron Multiplier
- ¹⁴⁵⁸ **HEED** High Energy Electro-Dynamics
- ¹⁴⁵⁹ **IEAP CTU** Institute of Experimental and Applied Physics, Czech Technical
¹⁴⁶⁰ University in Prague
- ¹⁴⁶¹ **IPC** Internal Pair Creation
- ¹⁴⁶² **EPC** External Pair Creation
- ¹⁴⁶³ **LArTPC** Liquid Argon TPC
- ¹⁴⁶⁴ **Micromegas** MICRO-MEsh GAseous Structure
- ¹⁴⁶⁵ **MPGD** Micro-Pattern Gaseous Detector
- ¹⁴⁶⁶ **MWPC** Multi-Wire Proportional Chamber
- ¹⁴⁶⁷ **OFTPC** Orthogonal Fields TPC
- ¹⁴⁶⁸ **PCB** Printed Circuit Board
- ¹⁴⁶⁹ **RK4** Runge-Kutta 4th order
- ¹⁴⁷⁰ **RPC** Resistive Plate Chamber
- ¹⁴⁷¹ **RPWELL** Resistive Plate WELL
- ¹⁴⁷² **THGEM** THick GEM
- ¹⁴⁷³ **ToA** time-of-arrival
- ¹⁴⁷⁴ **ToT** time-over-threshold
- ¹⁴⁷⁵ **TPC** Time Projection Chamber
- ¹⁴⁷⁶ **TPX3** Timepix3
- ¹⁴⁷⁷ **μ -PIC** Micro-Pixel Gas Chamber
- ¹⁴⁷⁸ **μ -RWELL** Micro-RWELL